Journal of
Applied Remote Sensing

RemoteSensing.SPIEDigitalLibrary.org

Remote sensing estimation of surface oil volume during the 2010 Deepwater Horizon oil blowout in the Gulf of Mexico: scaling up AVIRIS observations with MODIS measurements

Chuanmin Hu
Lian Feng
Jamie Holmes
Gregg A Swayze
Ira Leifer
Christopher Melton
Oscar Garcia
Ian MacDonald
Mark Hess
Frank Muller-Karger
George Graettinger
Rebecca Green

Chuanmin Hu, Lian Feng, Jamie Holmes, Gregg A Swayze, Ira Leifer, Christopher Melton, Oscar Garcia, Ian MacDonald, Mark Hess, Frank Muller-Karger, George Graettinger, Rebecca Green, "Remote sensing estimation of surface oil volume during the 2010 Deepwater Horizon oil blowout in the Gulf of Mexico: scaling up AVIRIS observations with MODIS measurements," *J. Appl. Remote Sens.* **12**(2), 026008 (2018), doi: 10.1117/1.JRS.12.026008.

SPIE.

Downloaded From: https://www.spiedigitallibrary.org/journals/Journal-of-Applied-Remote-Sensing on 16 Mar 2020
Terms of Use: https://www.spiedigitallibrary.org/terms-of-use

Remote sensing estimation of surface oil volume during the 2010 Deepwater Horizon oil blowout in the Gulf of Mexico: scaling up AVIRIS observations with MODIS measurements

Chuanmin Hu,[a,*] Lian Feng,[a] Jamie Holmes,[b] Gregg A Swayze,[c] Ira Leifer,[d] Christopher Melton,[d] Oscar Garcia,[e] Ian MacDonald,[f] Mark Hess,[g] Frank Muller-Karger,[a] George Graettinger,[h] and Rebecca Green[i]

[a]University of South Florida, College of Marine Science, St. Petersburg, Florida, United States
[b]Abt Associates, Boulder, Colorado, United States
[c]U.S. Geological Survey, Crustal Geophysics and Geochemistry Science Center, Denver, Colorado, United States
[d]Bubbleology Research International (BRI), Goleta, California, United States
[e]WaterMapping, LLC, Tallahassee, Florida, United States
[f]Florida State University, Department of Earth Ocean and Atmospheric Science, Tallahassee, Florida, United States
[g]Ocean Imaging, Littleton, Colorado, United States
[h]NOAA Ocean Service, Seattle, Washington, United States
[i]Bureau of Ocean Energy Management, Gulf of Mexico Region, New Orleans, Louisiana, United States

Abstract. The Deepwater Horizon (DWH) oil blowout in the Gulf of Mexico (GoM) led to the largest offshore oil spill in U.S. history. The accident resulted in oil slicks that covered between 10,000 and upward of 40,000 km^2 of the Gulf between April and July 2010. Quantifying the actual spatial extent of oil over such synoptic scales on an operational basis and, in particular, estimating the oil volume (or slick thickness) of large oil slicks on the ocean surface has proven to be a challenge to researchers and responders alike. This challenge must be addressed to assess and understand impacts on marine and coastal resources and to prepare a response to future spills. We estimated surface oil volume and probability of occurrence of different oil thicknesses during the DWH blowout in the GoM by combining synoptic measurements (2330-km swath) from the satellite-borne NASA Moderate Resolution Imaging Spectroradiometer (MODIS) and near-concurrent, much narrower swath (~5 km) hyperspectral observations from the NASA Airborne Visible/Infrared Imaging Spectrometer (AVIRIS). A histogram-matching approach was used to transfer AVIRIS-derived oil volume to MODIS pixel-scale dimensions, after masking clouds under both sun glint and nonglint conditions. Probability functions were used to apply the transformation to 19 MODIS images collected during the DWH event. This generated three types of MODIS oil maps: maps of surface oil volume, maps of relative oil thickness with four different classes (i.e., 0 μm, <0.08 μm, 0.08 to 8 μm, and >8 μm), and maps of probability distributions of different thicknesses. The results were compared with satellite-based synthetic aperture radar measurements and evaluated with concurrent aerial photographs. Although the methods may not be ideal and the results may contain large uncertainties, the current attempt suggests that coarse-resolution optical remote sensing observations can provide estimates of relative oil thickness/volume for large oil slicks captured by satellites. © *The Authors. Published by SPIE under a Creative Commons Attribution 3.0 Unported License. Distribution or reproduction of this work in whole or in part requires full attribution of the original publication, including its DOI.* [DOI: 10.1117/1.JRS.12.026008]

Keywords: Deepwater Horizon; oil spill; slick thickness; oil volume; Moderate Resolution Imaging Spectroradiometer; Airborne Visible/Infrared Imaging Spectrometer.

Paper 170960 received Nov. 11, 2017; accepted for publication Mar. 28, 2018; published online Apr. 27, 2018.

*Address all correspondence to: Chuanmin Hu, E-mail: huc@usf.edu

Downloaded From: https://www.spiedigitallibrary.org/journals/Journal-of-Applied-Remote-Sensing on 16 Mar 2020
Terms of Use: https://www.spiedigitallibrary.org/terms-of-use

1 Background and Objective: Mapping Surface Oil of the Deepwater Horizon Oil Blowout

The tragic Deepwater Horizon (DWH) blowout led to the largest accidental offshore oil discharge in the history of the modern petroleum industry. The estimates of oil volume released during the spill have varied widely, with the U.S. government providing an estimate of 3.19 million barrels of crude oil discharged into the northern Gulf of Mexico (GoM) over 87 days (20 April to 15 July 2010).[1–3] Government agencies, industry, and academic research groups collected an unprecedented amount of remote sensing observations of the surface ocean to help guide mitigation efforts and to assess the spatial extent and variations of oil on the surface of the GoM.[4] Studies have used different airborne and satellite sensors including satellite-based synthetic aperture radar (SAR),[5–7] Moderate Resolution Imaging Spectroradiometer (MODIS),[8–10] the Airborne Visible/Infrared Imaging Spectrometer (AVIRIS),[11–13] the Advanced Spaceborne Thermal Emission and Reflection Radiometer,[14–16] and the DMSC-MK2 UV-Visible-Near IR Sensor[17] to quantify oil extent on the ocean surface. Some of the imagery was used operationally by the U.S. National Oceanic and Atmospheric Administration (NOAA) and other groups to map the surface oil extent in order to provide timely information for oil tracking and mitigation.[9] An important challenge with remote sensing to date still needs to be addressed: How can surface oil thickness or volume be quantified through remote sensing?

NASA conducted extensive overflights with the scientific AVIRIS sensors during the evolution of the DWH event (Fig. 1). These observations were used to identify areas covered with

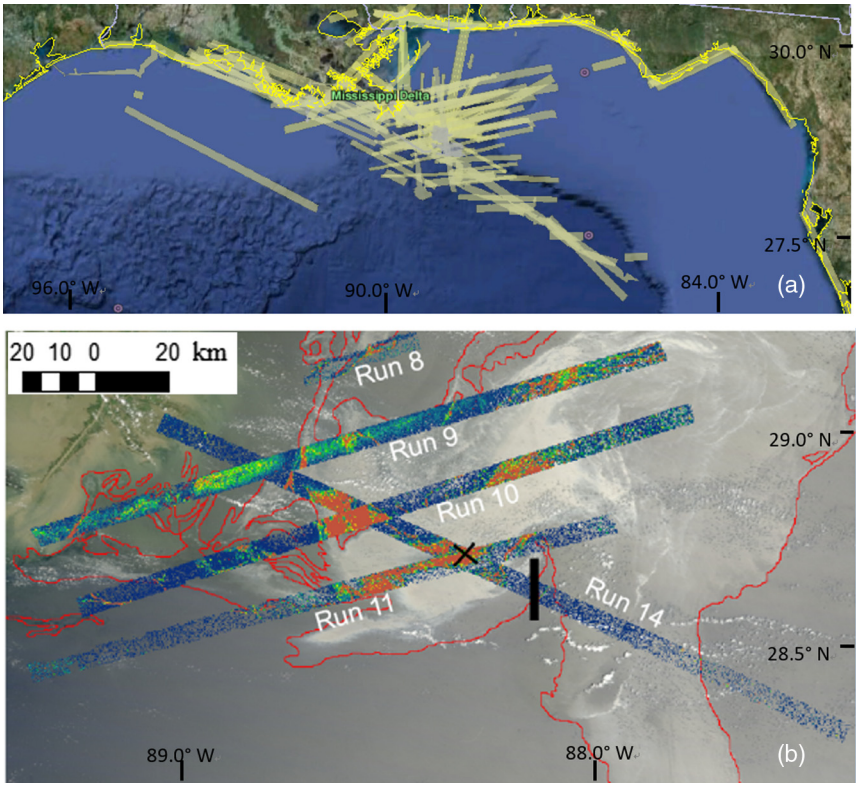


Fig. 1 (a) AVIRIS flight coverage in the northern GoM from May 6 to July 22, 2010. Coverage after July 22, 2010 is not shown here. A total of 456 flight lines in 41 days between May 6 and October 4, 2010 were surveyed by NASA JPL to assess the DWH oil spill. (b) However, to date, only the AVIRIS flight lines collected on May 17, 2010 have been processed by the USGS to generate surface oil volume estimates. These AVIRIS runs were used in this study to generate statistics to derive oil volume maps from MODIS. The background image in panel (b) shows the MODIS/terra red–green–blue (RGB) true color image collected on May 17, 2010.

Downloaded From: https://www.spiedigitallibrary.org/journals/Journal-of-Applied-Remote-Sensing on 16 Mar 2020
Terms of Use: https://www.spiedigitallibrary.org/terms-of-use

oil/water emulsions likely thicker than several dozens of microns.[4,12] AVIRIS oil volume data produced by Clark et al.[12] were used as the basis for the development of the empirical MODIS oil thickness model in this study. A limitation of sensors flown on aircraft is their limited spatial coverage, limited observation frequency, and ultimately, the significant effort required to analyze the data. Satellite-based sensors also were used extensively, as these provided data for quick surface oil presence/absence assessments. For example, the two MODIS sensors and MERIS together provided near-daily observations of the GoM at spatial resolutions of between 250 m and 1 km per pixel.

A fundamental problem with all remote sensing technologies is the difficulty in estimating thickness or volume of oil in a particular pixel. Additional information, external to that collected by one of these sensors, is required to differentiate between a <1 μm oil sheen and a >1 mm oil slick. Clearly, oil thickness is an important parameter needed to assess a spill's severity and to determine appropriate response actions. Improved oil characterization also provides insight into how different types of oil are transported in surface waters and informs federal agencies that perform oil spill risk analyses.

The challenges in estimating oil thickness on water are well documented.[18–20] Accurately measuring average oil thickness or volume from a vessel is challenging, given the difficulty of collecting data in the field and the spatial heterogeneity of oil.[17] During the DWH event, no scientific *in situ* measurements of oil thickness were made because there was no community-accepted method for such measurements, and no synoptic field sampling occurred when remote sensing data were collected. Regardless, to assess the impacts of the spill, government agencies needed to characterize the oil on the ocean surface, using the best information available. The wealth of different types of remote sensing data collected during the DWH blowout represents an opportunity to develop methods for quantifying oil thickness or volume using satellite-based remote sensing. The objectives of this study were to address this challenge through:

1. developing a method to scale up spatially limited but quantified oil thickness maps estimated from high-resolution hyperspectral AVIRIS measurements to multiband coarse-resolution MODIS observations;
2. developing a method to quantify the probability of oil coverage with different oil thickness at a given time and location;
3. mapping surface oil, its volume, classified by thickness, and the probability of different thickness classes.

Although these tasks are related, the methods used to achieve them are different. Therefore, unlike traditional manuscripts with one section for all Materials and Methods, this manuscript is arranged in the following way, where methods for different tasks are described separately. Below, we first provide a brief review of the remote sensing techniques needed to conduct oil spill assessments (Sec. 2). We then describe the approach to scale up AVIRIS oil volume estimates to larger spatial scales and conduct statistical assessments using MODIS measurements of surface reflectance (Sec. 3). We use AVIRIS-based statistics to generate probability functions of various oil thickness classes, and those statistics are then applied to the MODIS maps to generate probability coverage maps for different oil classes (Sec. 4). We compare the large-scale maps derived using MODIS to airborne photographs and to regional estimates of oil cover derived from satellite-based SAR observations (Sec. 5) and finally discuss uncertainties and weaknesses of our approach (Sec. 6). Diagnostic results are presented in Appendix A.

2 Remote Detection and Characterization of Surface Oil

Remote sensing techniques for oil spill detection and characterization include optical (both passive and active), microwave, thermal, lidar, and radar sensors mounted on aircraft and satellite platforms.[4,5,17,19,21,22] Merging the data from airborne and satellite sensors helps to scale up the high spatial resolution airborne measurements to conduct semiquantitative assessments of surface oil extent and oil volume over synoptic scales.

Downloaded From: https://www.spiedigitallibrary.org/journals/Journal-of-Applied-Remote-Sensing on 16 Mar 2020
Terms of Use: https://www.spiedigitallibrary.org/terms-of-use

SAR measurements have been used widely to detect the presence/absence of oil slicks, either by users manually delineating radar-dark areas, such as NOAA used during the DWH response (Environmental Response Management Application[23]), or using semiautomated data analysis schemes.[24] As part of the DWH analyses, combining concurrent data from multiple sensors, Garcia-Pineda et al.[5] recently demonstrated the possibility of identifying thick emulsified oil in SAR imagery. These data provide an excellent foundation with which to test new algorithms and methods.

Optical remote sensing provides useful, low-cost information on oil location and surface areal coverage.[25–31] Photographs collected with digital cameras and Landsat images proved the concept that visible radiance reflected off the ocean's surface provides information on oil seeps and spills.[30,32] Hu et al.[28] demonstrated the use of medium-resolution (250-m) MODIS data for spill assessment in Lake Maracaibo. Other studies have confirmed oil slick detection taking advantage of the sun glint in satellite images.[25,26,33] Figure 2 shows two MODIS images, taken only 1.5 h apart over the northern GoM, where oil slicks can be clearly visualized under sun glint [Fig. 2(a)] and nonglint conditions [Fig. 2(b)]. This optical contrast method was used operationally to trace the transport of DWH oil on surface of the GoM and to validate numerical models of the motion of the oil.[9,10,27] A combination of optical and SAR sensors can improve the coverage for spill monitoring and tracking.[7] In this paper, we develop the rationale to estimate thickness of the oil patches during the DWH blowout using optical means.

To date, attempts to estimate surface oil thickness and volume are based on empirical efforts, where relative oil thickness was assessed through visual inspection,[34] or relationships between laboratory measurements of reflectance spectra and known oil thickness were scaled to airborne and satellite observations.[17,35–38] Clearly, significant errors can be introduced. Laboratory conditions are typically for oil within a bottle, or at the surface of a container with a few squared meters in surface cross-section, which are different from the wide range of meteorological, oceanographic, and illumination conditions, where oil is over synoptic scales on the surface of the ocean. Indeed, the differences observed in an oil slick when viewed from different directions (Fig. 2) could be associated with the changes in solar and viewing geometry, rather than the changes in oil thickness or distribution. On the other hand, crude oil without emulsion[38] has dramatically different optical properties from oil emulsion:[12] the former shows large changes in reflectance in the blue–green wavelengths but negligible changes in the near-infrared (NIR) and short-wave infrared (SWIR) wavelengths, whereas the latter shows the opposite. In each case, reflectance does not change linearly with changing oil thickness. In the real ocean environment, surface oil can form oil emulsion (either water in oil or oil droplets in water) under influence of sun light and waves and therefore change reflectance over time,[39] making it difficult to develop unified rules to quantify nonemulsified oil and oil emulsion because the same amount of oil may be completely different reflectance magnitudes and shapes.

Radiative transfer modeling has been used to better understand the fundamental optics of oil–water interactions. Otremba et al.[40–43] developed a theoretical approach through

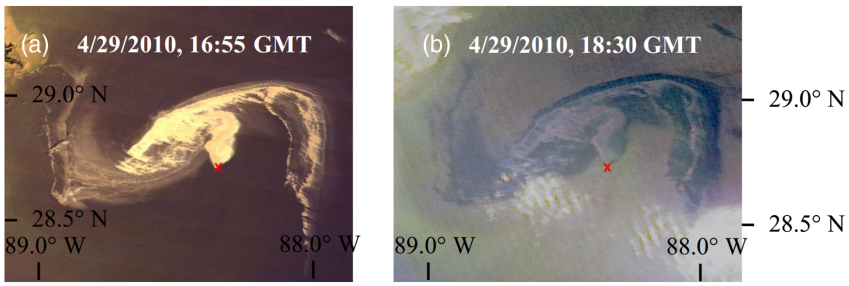


Fig. 2 MODIS RGB images (R: 645 nm; G: 555 nm; B: 469 nm) showing oil slicks with different optical contrast (spectral reflectance) only 1.5 h apart, due to different solar/viewing geometry and wind. (a) April 29, 2010, 16:55 GMT and (b) April 29, 2010, 18:30 GMT. The image width is about 120 km. The red X shows the DWH spill location. Figure adapted from Hu et al.[27]

Downloaded From: https://www.spiedigitallibrary.org/journals/Journal-of-Applied-Remote-Sensing on 16 Mar 2020
Terms of Use: https://www.spiedigitallibrary.org/terms-of-use

Monte-Carlo simulations to understand optical contrast of oil film and oil droplets under various conditions. This theoretical approach is currently not practical because it would require modelling observations and optical properties of both oil[38,44] and the underlying water[43] for all conditions encountered in each pixel of all satellite images covering an oil spill such as that of the DWH. Recently, an attempt was made to model reflectance of oiled surface under sun glint in order to determine oil slick thickness,[45] yet the general applicability of the approach remains to be tested.

A practical approach to estimate oil thickness was proposed by Clark et al.[12] They used hyperspectral laboratory measurements to develop algorithms for airborne hyperspectral images without sun glint. Unique spectral features in the shortwave-infrared (SWIR) wavelengths (e.g., at 1.2, 1.7, and 2.3 μm) are linked to different oil thickness and oil/water mixing ratios under controlled laboratory conditions. Based on these observations, Clark et al.[12] developed oil thickness maps from a few AVIRIS flight lines collected on May 17, 2010, including uncertainties in these estimates. More recently, Dubucq et al.[46] also demonstrated that SWIR wavelengths are useful for detecting thick oil slicks.

However, AVIRIS coverage for any particular day during the period of the DWH blowout was limited (Fig. 1). To date, only the analyses for flight lines on May 17, 2010 have been published.[12] MODIS provided more frequent optical observations at medium spatial resolution (250 and 500 m) during this time, often at near-daily temporal resolution. On May 17, 2010, MODIS observations were also collected nearly concurrently with AVIRIS flights. These data provide the basis to develop a systematic MODIS-based algorithm to combine the advantages of both measurements. MODIS and AVIRIS have important differences in spectral and spatial resolutions, as well as in their solar/viewing geometry. The objective of our study was to develop a simple and practical approach to overcome this technical challenge to improve assessments made with MODIS based on the limited AVIRIS observations and interpretations by Clark et al.[12] There are several data products derived from MODIS measurements, including oil volume maps, maps of oil thickness classes, and maps of oil probability. Each of these types uses its own method. Therefore, we describe these methods in a sequential way. Figure 3 presents a schematic flow chart to help understand the individual steps to derive the three data products (Products I to III), where the steps are detailed in the following sections.

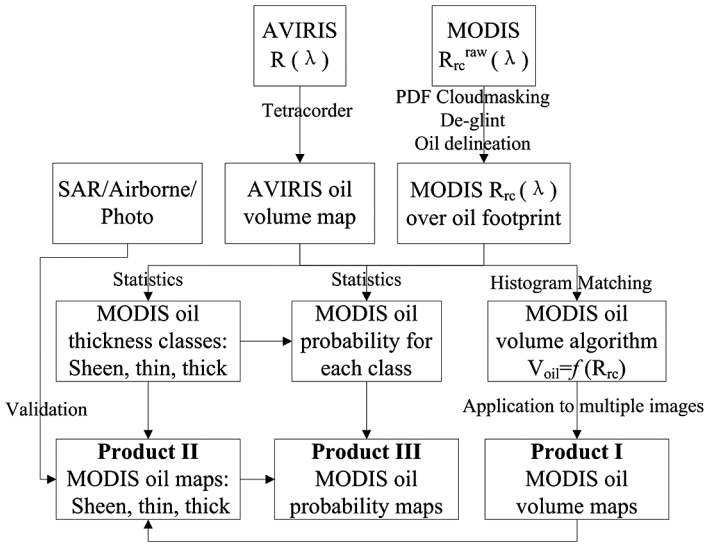


Fig. 3 Schematic flowchart showing the major steps in deriving the three MODIS-based data products (I to III). Product I is described in Sec. 3, while products II and III are described in Sec. 4 and validation is presented in Sec. 5. Here, AVIRIS $R(\lambda)$ refers to AVIRIS surface reflectance, MODIS R_{rc}^{raw} refers to the original MODIS Rayleigh corrected reflectance, and MODIS R_{rc} refers to R_{rc} anomaly of oil-containing pixels (in reference against nearby oil-free water pixel).

Downloaded From: https://www.spiedigitallibrary.org/journals/Journal-of-Applied-Remote-Sensing on 16 Mar 2020
Terms of Use: https://www.spiedigitallibrary.org/terms-of-use

3 Estimating Surface Oil by Spatially Scaling up AVIRIS Observations to Synoptic MODIS Measurements

3.1 *Data and Methods*

3.1.1 *Data sources and data processing*

The AVIRIS sensor has 224 spectral bands, from 380 to 2500 nm. Its ground resolution varies with aircraft altitude, generally between 3.5 and 20 m. AVIRIS data were collected on 41 days between May 6 and October 4, 2010, covering a total of 456 flight lines (Fig. 1). All the data are available in calibrated at-sensor radiances from the NASA Jet Propulsion Laboratory (Ref. 47).

The AVIRIS data collected on May 17, 2010, were processed by the USGS using the ACORN atmospheric correction module. Ground calibration sites were used to produce apparent surface reflectance [$R(\lambda)$, dimensionless]. Based on $R(\lambda)$, the USGS used the Tetracorder spectral shape-matching system[48] to derive oil/water mixing ratio, areal fraction coverage, thickness, and oil volume for each AVIRIS pixel containing thick oil emulsion.[12] The continuum-removed absorption feature strength and shapes for multiple absorption features were used by Clark et al.[12] to determine the oil:water ratio and oil volume. The observed level relative to the reference spectra for a specific oil:water ratio and volume was used to determine fractional coverage using a model with ocean water. The emulsions generated in the USGS laboratory from oil samples collected at the surface of the ocean during the DWH blowout were used to construct the relationships between sample properties (e.g., oil/water mixing ratios, effective oil thickness, oil volume) and reflectance spectral shapes and magnitudes in the SWIR bands.[12]

Three products were derived by Clark et al.[12] using the AVIRIS data: conservative, aggressive, and possible oil. In our study, we used the "aggressive" estimates to scale up MODIS observations because these were intermediate estimates (between the other two categories). These estimates then were used to derive subpixel fractional oil coverage for each MODIS image based on the near-concurrent AVIRIS observations of the same geographic area. Although termed "aggressive," the AVIRIS estimates did not include surface oil thinner than 20 μm because according to laboratory experiments, oil slicks thinner than 20 μm does not have reliably detectable SWIR signatures. Therefore, all subsequent MODIS analyses based on these AVIRIS results are regarded as an underestimate of the total DWH oil coverage and total volume at any particular time because the AVIRIS-derived estimates are used to scale the MODIS reflectance (Fig. 4).

MODIS collects spectral data in 36 bands from the visible to the thermal IR with nominal ground resolutions at nadir varying between 250 m and 1 km for different bands. In this study, the seven spectral bands designed for land and cloud observations were used because they do not saturate over sun glint regions.[49] These bands are 645 and 859 nm (250-m resolution); and 469, 555, 1240, 1640, and 2130 nm (500-m resolution).

The raw (level-0) MODIS data were obtained from NASA Goddard Space Flight Center (GSFC). Because the standard atmospheric correction (implemented in SeaDAS) often treats

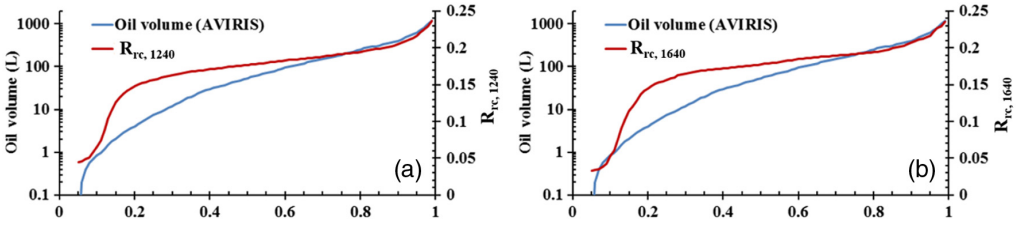


Fig. 4 Cumulative histograms of MODIS Rayleigh-corrected reflectance (a) $R_{rc,1240}$ (aqua) and (b) $R_{rc,1640}$ (terra; both after subtraction of the nearest water background), and AVIRIS-derived surface oil volume for the AVIRIS flight line Run10 in Fig. 1(b). The *x*-axis shows the cumulated frequency. Note that oil volume is plotted in log scale. They show different shapes in the cumulative histograms but are forced to agree with each other at each *x*-axis point using regressions, as shown in Fig. 5.

Downloaded From: https://www.spiedigitallibrary.org/journals/Journal-of-Applied-Remote-Sensing on 16 Mar 2020
Terms of Use: https://www.spiedigitallibrary.org/terms-of-use

the bright pixels (from either weathered oil or sun glint) as clouds or bad data, SeaDAS was used only to derive the calibrated top of atmosphere sensor radiance ($L_{t,\lambda}$). Then, Rayleigh-corrected reflectance for each band [$R_{rc,\lambda}^{raw}$] was derived as per Hu et al.:[26]

$$R_{rc,\lambda}^{raw}(\theta_0,\theta,\Delta\phi) = \pi L^*_{t,\lambda}(\theta_0,\theta,\Delta\phi)/(F_{0,\lambda}\times\cos\,\theta_0) - R_{r,\lambda}(\theta_0,\theta,\Delta\phi), \quad (1)$$

where L^*_t is L_t after correction for gaseous absorption, F_0 is the extraterrestrial solar irradiance, θ_0 is the solar zenith angle, θ is the sensor zenith angle, $\Delta\phi$ is the relative azimuth between the sensor and the sun, and R_r is the reflectance due to Rayleigh (molecular) scattering. The solar-viewing geometry is defined by $(\theta_0,\theta,\Delta\phi)$, which changes from pixel to pixel. The $R_{rc,\lambda}^{raw}$ data were mapped to a rectangular projection at 250-m resolution covering the GoM or a georeferenced window covering particular oil features. During this step, the 500-m resolution data were interpolated to 250-m resolution using a sharpening scheme.[50] The bands centered at 645, 555, and 469 nm were used to compose true-color red–green–blue (RGB) images for visualization. Here, the superscript "raw" indicates that these are the raw R_{rc} data from direct Rayleigh correction. In the subsequent analysis, the R_{rc}^{raw} data over oil-containing pixels are referenced against nearby oil-free water, resulting in reflectance anomaly. Such an oil–water anomaly is referred to as R_{rc} (Fig. 4).

3.1.2 *Methods for deriving MODIS oil thickness maps*

Delineate surface oil slicks. The step-by-step details in the processing and delineation of the oil patterns at the surface of the ocean are described in the International Ocean Color Coordinating Group (IOCCG) handbook.[27] We briefly summarize the method below.

Oil on the surface of the ocean shows spatial contrast (either positive or negative, or both) with surrounding background water in MODIS R_{rc} imagery with sun glint. This allows slicks to be delineated.[8,25,26] This step effectively provides a measure of oil presence or absence on the surface for each pixel. Whereas several image segmentation (classification) methods have been established to delineate slicks in a semiautomatic fashion,[24] such methods are not effective with MODIS sun glint imagery because the intensity of the sun glint is uneven across any one image, different from image to image, and because clouds interfere with the observed spatial patterns.[51] Therefore, manual delineation is more effective to outline the boundary of each slick after interactive image stretching to highlight the oil–water contrast.[26] An example is shown in Fig. 1(b), where the slick delineation is shown in red. In the work of Hu et al.,[29] about 50 MODIS images between April 22 and July 31, 2010, were used to study the presence of oil in the northeastern GoM, where the aggregated oil footprint was determined to be 103,000 km^2.

In the present work, after screening for cloud cover, we selected a dataset consisting of 19 images spanning 18 days (Table 1; note that we used two images collected on April 29, 2010). These represent the best cloud-free MODIS data.

Cloud masking. Clouds are opaque to light and therefore need to be identified in optical remote sensing imagery and removed from further processing to minimize errors in estimating surface ocean oil cover. We tested several cloud-masking methods for the present study but none gave entirely satisfactory results. These include the standard MODIS cloud mask (MOD35),[52] and cloud mask strategies we developed for our sea surface temperature (SST) data product and for MODIS sun glint imagery.[8] These methods resulted in either too many false-positive pixels (i.e., too many pixels labeled as clouds) or too many false-negative pixels (i.e., too many clouds missed). For example, the MOD35 cloud mask often identified thick oil as clouds (Fig. 17) in Appendix A1).

We therefore developed a cloud masking method specifically to address this issue for this study using a probability density function (PDF). The PDF was used to examine pixels within a running window for texture analysis (see Appendix A1 for more details). This method led to a much improved set of cloud masks, as shown, for example, in Appendix A1 (Fig. 17).

Downloaded From: https://www.spiedigitallibrary.org/journals/Journal-of-Applied-Remote-Sensing on 16 Mar 2020
Terms of Use: https://www.spiedigitallibrary.org/terms-of-use

Table 1 MODIS images and estimated total surface oil volume (units: 10^3 barrels). Total oil volume was estimated from (1) continuous oil volume maps (continuous), which is "product I" in Fig. 3; (2) probability maps using three MODIS thickness classes (probability_three), which is "product III" in Fig. 3; and (3) probability maps using five MODIS thickness classes (probability_five), which is also "product III" in Fig. 3. The meaning of these three different estimates is explained in the following sections. The image name convention is SYYYYMMDD.HHMMSS, where S: sensor (A: MODIS/aqua; T: MODIS/terra), YYYY: year, MM: month, DD: day, HH: GMT hour, MM: minutes, SS: seconds. The decreases in oil volume over time (e.g., after day 20000527) can be due to mitigation efforts and/or storms.[7]

	Continuous (10^3 barrels)	Probability_three (10^3 barrels)	Probability_five (10^3 barrels)
A20100425.185500	27	30	33
T20100429.165500	49	51	52
A20100429.183000	49	57	62
A20100504.184500	78	74	75
A20100509.190500	106	55	55
T20100510.163500	111	82	85
A20100511.185500	117	89	93
T20100517.164000	150	130	124
A20100520.184500	167	210	239
A20100523.191500	184	251	272
T20100524.164500	190	214	228
A20100527.185510	206	299	346
A20100610.190500	156	165	170
A20100612.185010	210	145	160
T20100618.164000	174	158	168
A20100626.190500	146	154	159
A20100712.190500	45	45	47
A20100714.185500	67	84	90
A20100721.190000	52	83	88

The PDF-generated cloud mask for each of the 19 MODIS images was carefully inspected and cross-referenced with the corresponding MODIS RGB image. Small artifacts occurred infrequently in the PDF cloud mask product, as one can easily tell which pixels were clouds from the RGB image because clouds are features that stand out from the background pixels and clouds often have shadows in adjacent pixels. Small cloud patches were sometimes missed while some other cloud-free pixels were treated as clouds. These rare (<5%) artifacts were manually corrected, resulting in a final dataset of cloud masks. These were applied to the MODIS images (i.e., masking the corresponding pixels) prior to performing statistical analyses.

After application of the cloud mask, $R_{rc,\lambda}^{raw}$ was used to delineate the oil presence/absence based on their spatial contrast with the surrounding waters. To minimize the effects of sun glint, the R_{rc}^{raw} value of each oil pixel was normalized by subtracting a mean R_{rc}^{raw} value of the nearest oil-free water pixels, where these pixels were determined through comparing

Downloaded From: https://www.spiedigitallibrary.org/journals/Journal-of-Applied-Remote-Sensing on 16 Mar 2020
Terms of Use: https://www.spiedigitallibrary.org/terms-of-use

the distance of water pixels to the oil-pixel of interest.[53] Such deglinted R_{rc} values represent the oil–water R_{rc} contrasts, which also corrected the aerosol scattering effects through the reference subtraction. In the following text, $R_{rc,\lambda}$ refers to the oil–water reflectance anomaly. We then proceeded to estimate average oil thickness as oil volume contained in each oil pixel based on the $R_{rc,\lambda}$ product using the AVIRIS observations described in the following section.

Correlation between MODIS and AVIRIS. We tested several methods to examine the relationship between MODIS $R_{rc,\lambda}$ data and AVIRIS reflectance data, and to build an empirical model of using MODIS $R_{rc,\lambda}$ data to estimate surface oil volume, based on concurrent and colocated AVIRIS oil volume data. We first had to account for the different spatial resolution (pixel size) of the MODIS and AVIRIS images and the different measurement conditions associated with each sensor. For example, MODIS images may show sun glint, whereas AVIRIS images were collected in a way that purposefully minimized sun glint. We concluded that a pixel-to-pixel match between MODIS and AVIRIS, even after aggregating AVIRIS pixels to the MODIS pixel size, simply did not provide a solid base for the empirical model of surface oil volume (see Appendix A2). This can be due to the fact that there may have been a location mismatch between AVIRIS and MODIS measurements (AVIRIS ~ 20:00 GMT while MODIS ~ 16:40 GMT). We therefore developed and tested a histogram-matching strategy, as outlined below. Note that histogram matching in typical image processing is a process whereby an image is transformed so that its histogram matches that of a specified histogram. Here, we simply use the term to force two histograms from MODIS $R_{rc,\lambda}$ and AVIRIS-derived oil volume, respectively, to agree with each other. In such a method, slight mismatch in locations of oil slicks between AVIRIS and MODIS would not result in a significant problem as total oil volume from the two measurements should be similar. This is clearly evidenced in the MODIS image pairs in Fig. 2, which were collected 1.5 h apart with very similar spatial distribution patterns.

With histogram matching, the cumulative histograms from MODIS R_{rc} and from AVIRIS-derived oil volume were forced to agree with each other. By testing different MODIS bands, we found that the 1640-nm band from MODIS/Terra and the 1240-nm band from MODIS/Aqua provided the most sensitive histograms relative to the AVIRIS cumulative oil volume histograms because of the elevated reflectance of thick emulsified oil in these spectral bands.[12] Different bands were selected for MODIS/Terra and MODIS/Aqua because of the detector errors in the MODIS/Terra 1240-nm band and MODIS/Aqua 1640-nm band. The 2130-nm bands have much lower sensitivity (signal-to-noise ratio) and therefore were not used.[49] Figure 4 shows the cumulative histograms for MODIS R_{rc} in these bands and AVIRIS-derived oil volume for the entire AVIRIS flight line Run10 shown in Fig. 1(b).

Both Figs. 4(a) and 4(b) show similar curve shapes in the cumulative histograms for the deglinted $R_{rc,1240}$ and $R_{rc,1640}$ values. To show low oil volume more effectively, the y-axis in the figures was plotted in log scale. As with any cumulative histograms, the monotonously increasing patterns in both MODIS R_{rc} and AVIRIS oil volume can be used to establish a relationship between the two. Such relationships are shown in Figs. 5(a) and 5(c) for MODIS/Terra and MODIS/Aqua, respectively. Polynomial regressions were obtained between the two parameters. Using such regression relationships derived for the May 17, 2010 AVIRIS and MODIS measurements, MODIS R_{rc} data for all images were used to model oil volume for each MODIS pixel.

We compared the oil volume modeled from MODIS R_{rc} with the oil volume estimates from the corresponding overlapping AVIRIS images [Figs. 5(b) and 5(d)]. We found excellent agreement between the two; this was expected since the model uses a self-tuning approach to force the two observations to agree with each other. For the same reason, Fig. 5 does not mean that there is a definitive relationship between MODIS R_{rc} and oil volume for the individual MODIS pixels. Instead, for a given MODIS R_{rc} value, the integrated oil volume for all MODIS pixels below that R_{rc} value agrees with the integrated oil volume for all corresponding AVIRIS pixels in

Downloaded From: https://www.spiedigitallibrary.org/journals/Journal-of-Applied-Remote-Sensing on 16 Mar 2020
Terms of Use: https://www.spiedigitallibrary.org/terms-of-use

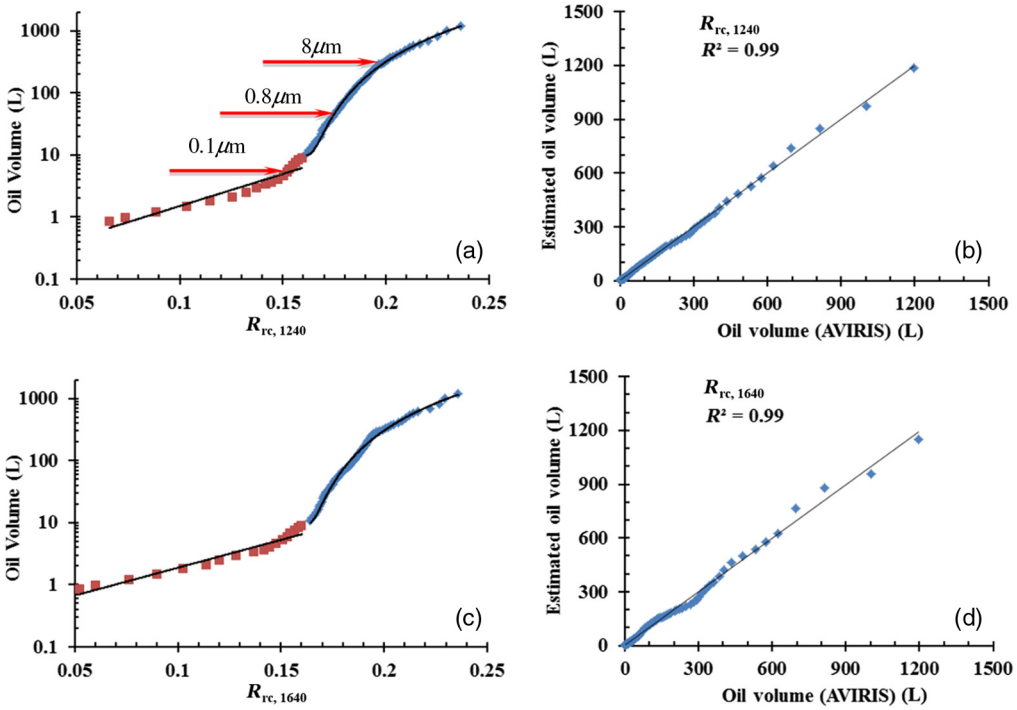


Fig. 5 Histogram-matching relationships between AVIRIS-derived oil volume and MODIS (a) $R_{rc,1640}$ (terra) and (c) $R_{rc,1240}$ (aqua). The relationships are based on the histograms shown in Figs. 4(a) and 4(b), respectively. The black lines are stepwise polynomial regressions. These led to MODIS-derived oil volumes in (b) and (d) (*y*-axis), as compared with AVIRIS-derived oil volume (*x*-axis) for this particular case on May 17, 2010. These regressions were applied to all MODIS images (both terra and aqua) under similar sun glint conditions to derive oil thickness maps. The arrow annotations in panel (a) show the average thickness per pixel that corresponds to the oil volumes shown in the *y*-axis. In this study, MODIS-derived oil volume maps were classified into one of these three bins.

order to have mass conservation. The regression results should be interpreted as multipixel statistics rather than at individual pixel level.

In the rest of the text below, we refer to the relationship between MODIS R_{rc} under sun glint and surface oil volume as $R_{rc}^{glint} - V$ regressions.

Consistency between MODIS observations collected under different conditions. The algorithms derived from the histogram matching between AVIRIS and MODIS should only be applied to MODIS images collected under similar sun glint conditions. Some of the MODIS images do not contain significant sun glint [e.g., Fig. 2(b)]. An alternate approach was required to estimate oil volume (or average thickness) under different sun glint conditions.

Based on the same idea of deriving $R_{rc}^{glint} - V$ relationships between AVIRIS and MODIS images, we derived a relationship between MODIS R_{rc} with sun glint [Fig. 2(a)] and without sun glint [Fig. 2(b)]. To minimize the impact of possibly different atmospheric aerosols (type and quantity) and illumination between the scenes, again the R_{rc} data were those normalized against the nearest oil-free water pixels for both MODIS images.

Figures 6(a) and 6(b) show the R_{rc} histograms for the MODIS images without sun glint [Fig. 2(b)] and with sun glint [Fig. 2(a)], respectively. The relationship between their R_{rc} after histogram matching is shown in Fig. 6(c). Such derived relationships were applied to the $R_{rc}^{glint} - V$ relationships, resulting in the correlation between surface oil volume and MODIS R_{rc} under nonglint conditions (termed as $R_{rc}^{no\text{-}glint} - V$ thereafter).

Downloaded From: https://www.spiedigitallibrary.org/journals/Journal-of-Applied-Remote-Sensing on 16 Mar 2020
Terms of Use: https://www.spiedigitallibrary.org/terms-of-use

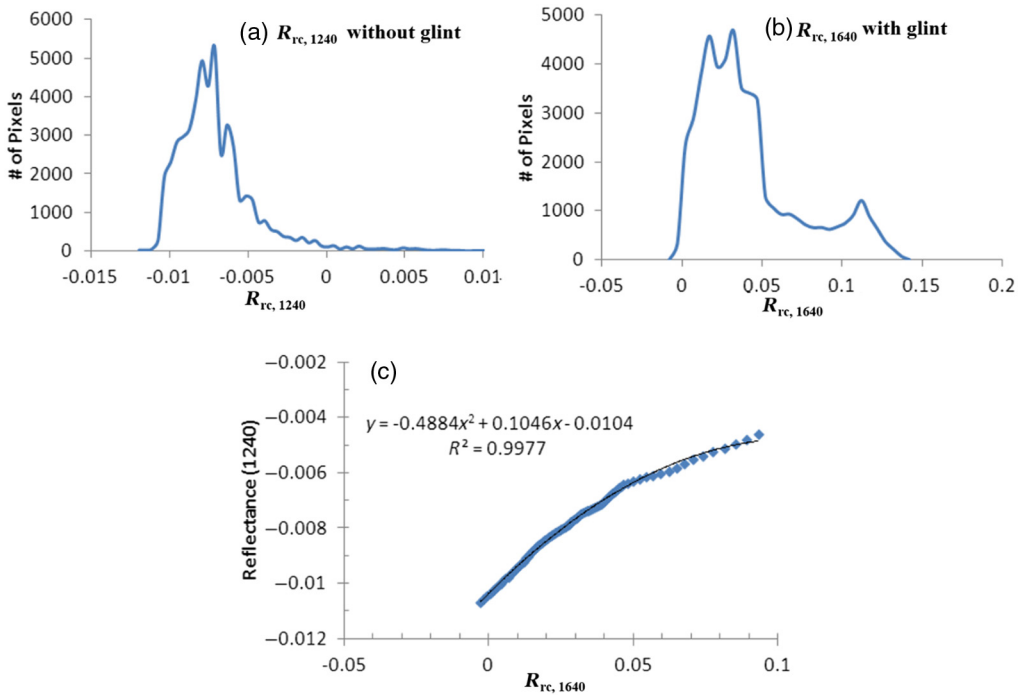


Fig. 6 Histogram match between MODIS oil pixels delineated under (a) no sun glint and (b) sun glint conditions from aqua and terra measurements on April 29, 2010 (see Fig. 2), respectively. Note that after the nearest-neighbor correction, most reflectance values from the oil pixels are negative in (a), meaning that pixels with oil are darker than the surrounding water when no sun glint is present. The 1240-nm and 1640-nm bands are chosen for MODIS/aqua and MODIS/terra, respectively, because of bad detectors for the MODIS/aqua 1640-nm band and MODIS/terra 1240-nm band. The regression relationship derived from the histogram match is shown in panel (c).

Application to MODIS observations. The 19 MODIS images in Table 1 were separated into two classes: with sun glint, where oil slicks show positive spatial contrast from the surrounding water [e.g., Fig. 2(a)], and without sun glint, where oil slicks show both positive and negative contrasts [e.g., Fig. 2(b)] at visible wavelengths. For sun glint and nonsun glint cases, $R_{rc}^{glint} - V$ and $R_{rc}^{no\text{-}glint} - V$ regressions were used to derive the oil volume maps, respectively. The regression relationships were applied to pixels delineated as containing oil, after appropriate cloud masking (Fig. 3).

3.2 *MODIS Oil Thickness Maps*

Figure 7 shows an example of the MODIS derived oil volume distribution on May 17, 2010. For a fixed pixel size (250 m × 250 m), the oil volume shown in Fig. 7(b) can be converted to average thickness per pixel. Visual inspection indicates that there is a general relationship between MODIS brightness and oil volume (i.e., oil volume increases with increasing reflectance). This is a result of the $R_{rc}^{glint} - V$ regression. Some of the changes in MODIS brightness are apparently due to other factors than surface oil. For example, along the tail of the oil slick to the southeast of the blowout site, there is a very bright patch. This may be caused by current shears due to a cyclonic eddy north of the tail and an anticyclonic eddy (i.e., the loop current) south of the tail. Direct application of the regression relationship to the delineated patch would result in an overestimate of the oil volume. Thus, the oil patches along the tail were manually changed to no value (i.e., no valid observation).

Figures 8 and 9 show two other examples of such MODIS-derived oil volume maps under similar sun glint conditions. The oil volume maps indicate substantial spatial structure of the

Downloaded From: https://www.spiedigitallibrary.org/journals/Journal-of-Applied-Remote-Sensing on 16 Mar 2020
Terms of Use: https://www.spiedigitallibrary.org/terms-of-use

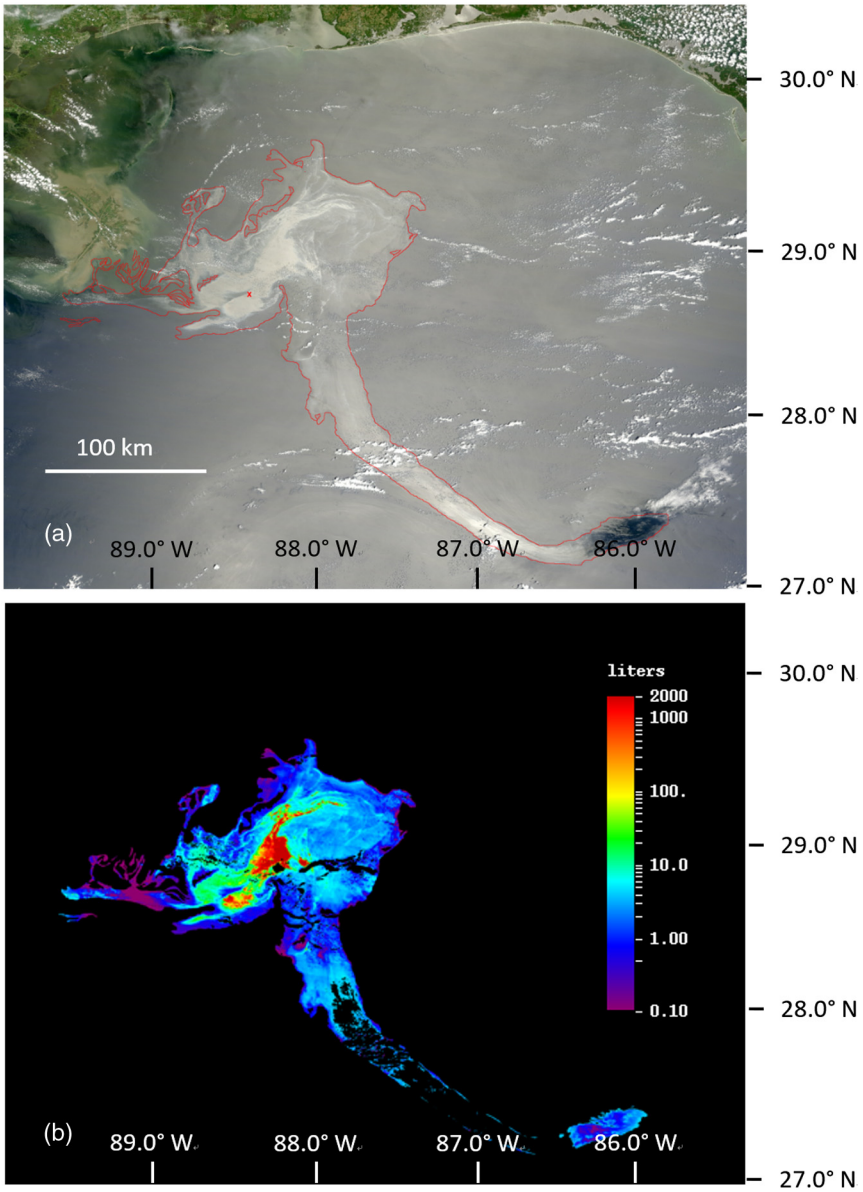


Fig. 7 (a) MODIS Terra 250-m resolution RGB image on May 17, 2010 showing oil slicks (outlined in red) from the DWH oil spill. This is the same image as in Fig. 1(b). The oil slicks outlined in red have enhanced contrast due to both sun glint and water circulations; (b) surface oil volume map derived from the MODIS R_{rc} data using the AVIRIS-MODIS regression relationship and some manual cleanup of anomalies ($R_{rc}^{glint} - V$ regression; see text). This type of map is listed as "product I" in Fig. 3. The color-coded numbers represent estimated surface oil volume per MODIS 250-m pixel (note that the MODIS pixel in the E-W direction is adjusted by cosine of latitude after map projection, corresponding to ~223 m). 1000 L/pixel is approximately equivalent to a uniform 18 μm in oil thickness, and likewise, 100 L/pixel is approximately equivalent to a 1.8 μm in oil thickness. The relatively low thickness is due to mixed pixels.

surface oil patches. For example, the western part of the oil slick in Fig. 8(c) (i.e., left half of the slick) shows thicker patches than the eastern part of the slick. This is reasonable, since the western side is closer to the DWH spill site. Such enhanced reflectance can even be detected by the low-SNR meteorological GOES Imager under nonglint conditions.[54]

The $R_{rc}^{no\text{-}glint} - V$ regression was applied to MODIS images, where oil slicks showed negative contrast relative to open waters (Fig. 10). The oil volume map derived by Terra image under sun glint conditions 1.5 h earlier, analyzed using $R_{rc}^{glint} - V$ regression [Fig. 9(b)],

Downloaded From: https://www.spiedigitallibrary.org/journals/Journal-of-Applied-Remote-Sensing on 16 Mar 2020
Terms of Use: https://www.spiedigitallibrary.org/terms-of-use

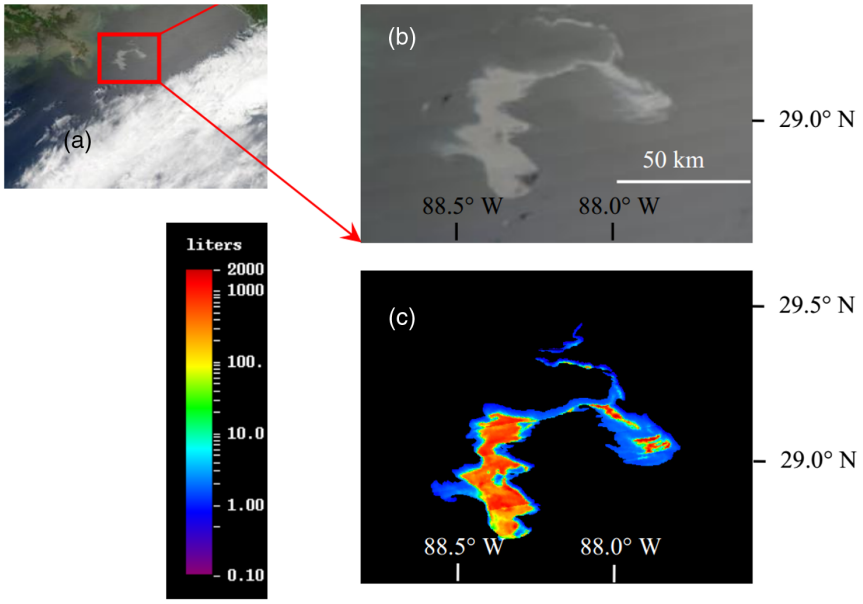


Fig. 8 Same analysis as in Fig. 7, but the MODIS Aqua RGB images in (a) and (b) and oil volume map in (c) were from April 25, 2010 (18:55 GMT). The color-coded numbers represent estimated surface oil volume per MODIS pixel. 1000 L/pixel is approximately equivalent to 18 μm in oil thickness, and likewise, 100 L/pixel is approximately equivalent to 1.8 μm in oil thickness.

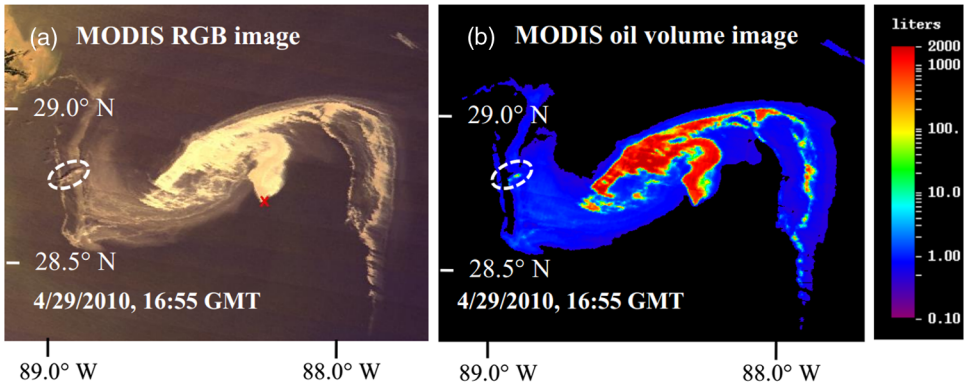


Fig. 9 (a) MODIS Terra RGB image collected on April 29, 2010, at 16:55 GMT and (b) the corresponding MODIS oil volume image (i.e., "product I" in Fig. 3). The high-concentration patch outlined by the dotted circle in (b) is apparently due to contamination by clouds. 1000 L/pixel is approximately equivalent to 18 μm in oil thickness, and likewise, 100 L/pixel is approximately equivalent to 1.8 μm in oil thickness.

shows comparable spatial patterns for most of the spilled region. To the left of the image (southwest portion of the spill), there were some inconsistencies between the two volume images. Figure 9(b) shows thin oil films but Fig. 10(b) shows several thick slicks. Such inconsistencies may be due to changes over time and other possible causes for which the method may not account.

Table 1 provides a summary of the total surface oil volume derived from the 19 MODIS images, termed as "product I" in Fig. 3. During the month after the initial blowout, total oil volume increased almost monotonically. After May 27, 2010, total oil volume at the surface remained relatively stable except on June 12. Some of the physical and chemical processes that played a role in modulating the surface oil volume were discussed by MacDonald et al.[7]

Downloaded From: https://www.spiedigitallibrary.org/journals/Journal-of-Applied-Remote-Sensing on 16 Mar 2020
Terms of Use: https://www.spiedigitallibrary.org/terms-of-use

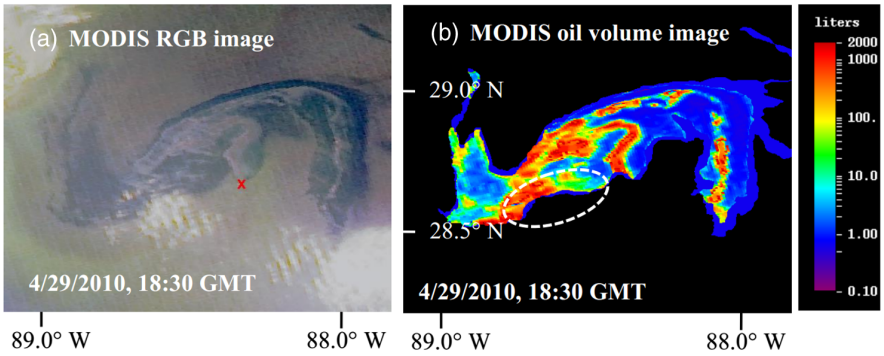


Fig. 10 (a) MODIS Aqua RGB image collected on April 29, 2010, at 18:30 GMT. (b) The corresponding MODIS oil volume image (i.e., "product I" in Fig. 3). The high-concentration patch outlined by the dotted circle in (b) is apparently due to contamination by clouds. The color-coded numbers represent surface oil volume per MODIS pixel. 1000 L/pixel is approximately equivalent to 18 μm in oil thickness, and likewise, 100 L/pixel is approximately equivalent to 1.8 μm in oil thickness. Note that the image in (a) is the same as in Fig. 2(b).

4 Oil Classification and Probability Maps

4.1 *Methods*

The time series of MODIS images shows oil volume estimates that rarely exceeded 1000 L per 250 m pixel, corresponding to an average thickness of 18 μm. The maximum estimated oil volume per pixel was around 2000 L or an average thickness of 36 μm. DWH oil response and recovery efforts focused on surface oil that was thick (>1 mm).[7,36] Observations from AVIRIS, boats, and laboratory-based spectral measurements indicated that surface oil thickness indeed reached several millimeters to >1 cm in extreme cases.[12]

Our upper limit of thickness from the MODIS-based estimates appears lower than is actually observed in the field. This apparent discrepancy is mainly due to pixel size. Surface oil can be very patchy, and only a small area within a MODIS pixel had thick oil. Although the NIR-SWIR reflectance of thick oil may be saturated beyond a certain thickness (e.g., a few millimeters),[12] this is unlikely to happen to the entire AVIRIS 7.6-m pixels and such a saturation effect would not impact the fact that the MODIS signal is confounded with both thick and thinner patches for a reduced mean thickness over the area of the MODIS pixel. This effect is illustrated in Fig. 21 and in Sun et al.,[11] where within a MODIS pixel, some AVIRIS pixels can have much thicker oil than the mean oil thickness of the MODIS pixel. Indeed, based on AVIRIS measurements, Sun et al.[11] estimated that if 50% fractional pixel coverage were to be required to detect oil with thickness greater than sheen for most oil containing pixels, a 30-m resolution sensor would be needed.

In practice, for the same oil volume within a MODIS pixel, the impact to the marine environment may be different between two scenarios: the pixel contains homogeneous oil films of 5 μm or heterogeneous oil films of varying thickness (e.g., from submicrons to millimeters) with their average being 5 μm. Assessment of thick oil distributions may be particularly important for oil spill assessment, as ocean plants (e.g., pelagic *Sargassum spp.*) and animals (fish, birds) may be significantly affected at scales much smaller than the MODIS pixel size.

To better understand the oil patchiness and uncertainty in average oil thickness estimated with MODIS, two methods were used to modify the MODIS-derived oil volume maps (Fig. 3).

The first method divided the features identified in each image into several oil thickness classes, specifically thin, medium, and thick. The Bonn Agreement[55] provides five thickness codes to describe different thickness ranges. These were based on field observations, where observed areas are much smaller than MODIS pixels. If these classes were to be used, there would be no MODIS pixels in the two thickest classes. Therefore, three oil thickness classes were defined according to MODIS oil volume histograms shown in Fig. 5(a).

Downloaded From: https://www.spiedigitallibrary.org/journals/Journal-of-Applied-Remote-Sensing on 16 Mar 2020
Terms of Use: https://www.spiedigitallibrary.org/terms-of-use

In Fig. 5(a), there are two inflection points, corresponding to oil thickness of 0.08 and 8 μm, respectively. Then, the three classes of oil thickness were chosen as: <0.08 μm (but >0, representing oil sheen), between 0.08 and 8 μm, (representing thin oil), and >8 μm (representing thick oil). The oil volume maps derived in Sec. 3 were first converted to thickness maps, from which three classes were separated on each map.

A second method was to derive oil probability maps. Oil probability distribution analyses allow estimates of the likelihood that oil of a given thickness will occur in a MODIS pixel. Integration of the probabilities allows an estimate of total volume within a pixel.

Three steps are required to convert average thickness to probability values for different thickness classes. Step 1 was to define the thickness classes. Three thickness classes were defined following the Bonn Agreement and AVIRIS statistics. The three classes have thickness ranges of about: >0 to <1.7 (mean ~ 1 μm), 1.7 to 20 μm (mean ~ 10 μm), and >20 μm (mean ~ 50 μm) (Table 2). The basis for such selections can be found in Appendix A4. Note that these thickness classes are from AVIRIS statistics instead of MODIS statistics.

Step 2 was to define the probability functions for each MODIS thickness class (<0.08 but >0 μm; 0.08 to 8 μm; >8 μm). This is accomplished by examining AVIRIS oil thickness statistics (derived from this study) for each MODIS thickness class. For the data on May 17, 2010, the AVIRIS pixels had a resolution of 7.6 m. Thus, for each 250-m MODIS pixel collected at the same time, AVIRIS had over 1000 pixels of data. These data show that a MODIS R_{rc} classified as thin oil (for example) in fact may have patches of oil at the 7.6-m scale that cover a wide range of thicknesses. Figure 11 shows the cumulative AVIRIS statistics for each MODIS class. Even for the thin MODIS class, there are still some AVIRIS pixels with oil thickness >50 μm. In other words, for each MODIS class, there are fractional areas with different oil thicknesses. These thicknesses are defined as 1, 10, 50 μm with their corresponding ranges >0 to <1.7 μm, 1.7 to 20 μm, and >20 μm. In calculating statistics, AVIRIS pixels containing no oil were included. After this was taken into account, the probability of each of the four AVIRIS thickness classes (including 0 μm) within each MODIS class was calculated (Table 3). For example, for a MODIS pixel classified to contain oil of median thickness (0.08 to 8 μm), on average 87.2% of the pixel contains no oil, 0.0031% contained oil of 1 μm, 0.5% contained oil of 10 μm, and 12.3% contained oil of 50 μm.

These data illustrate the spatial heterogeneity of the oil within a MODIS pixel. A typical MODIS pixel covering the detected oil had patches of thick oil, and the remainder of the area had either no oil or very thin oil (AVIRIS was not used to classify thin sheens).

Table 2 The Bonn Agreement (2012) on oil appearance and thickness classes together with MODIS oil thickness classes and AVIRIS thickness classes defined in this study (modified from those determined by Clark et al.)[12]. These are based on statistics of MODIS and AVIRIS. The choice of the three MODIS classes and the sensitivity of integrated oil volume on the different threshold choices can all be found in Appendix A4. Note the different names in the thickness classes.

Bonn Agreement			This study			
Code	Description/appearance	Thickness (μm)	MODIS class	MODIS thickness (μm)	AVIRIS class	AVIRIS thickness (μm)
1	Sheen	0.04 to 0.3	Sheen	<0.08	Thin	<1.7 μm (mean ~ 1 μm)
2	Rainbow	0.3 to 5.0	Thin	0.08 to 8 μm		
3	Metallic	5.0 to 50	Thick	>8 μm	Thick	1.7 to 20 μm (mean ~ 10 μm)
4	Discontinuous True Color	50 to 200			Thicker	>20 μm (mean ~ 50 μm)
5	Continuous True Color	>200				

Downloaded From: https://www.spiedigitallibrary.org/journals/Journal-of-Applied-Remote-Sensing on 16 Mar 2020
Terms of Use: https://www.spiedigitallibrary.org/terms-of-use

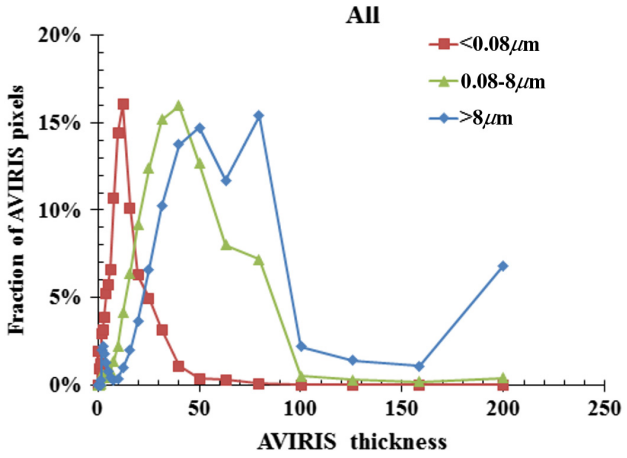


Fig. 11 Probability of AVIRIS thickness (in micrometers) distributions after they are aggregated to MODIS pixel sizes for the three MODIS classes (>0 but <0.08 μm, 0.8 to 8 μm, and >8 μm). All AVIRIS data from Fig. 1(b) were used in the calculations. The aggregation included both oil and oil-free AVIRIS pixels.

Table 3 Fractional coverage of oil with different thicknesses (first row, determined from AVIRIS statistics and Bonn agreement) in each MODIS thickness class (first column). The AVIRIS classes (0, 1, 10, 50 μm) correspond to the following ranges (0, >0 but <1.7, 1.7 to 20, >20 μm). These statistics are based on all AVIRIS flight lines on May 17, 2010. For example, for the MODIS pixels classified as containing oil of 0.08 to 8 μm thick, 87.2% of their covered surface contain no oil, and 12.28% of their covered surface contain thick (50 μm) oil.

	AVIRIS thickness class			
MODIS thickness class	0 μm	1 μm	10 μm	50 μm
0 μm	1.0	0	0	0
<0.08 μm	0.998	9.30E-05	0.00195	0.0004
0.08 ~ 8 μm	0.872	3.10E-05	0.00507	0.1228
>8 μm	0.612	0.000136	0.13567	0.2519

Step 3 was to apply these established probability functions (Table 3) to the MODIS classification maps to derive oil probability maps. In doing so, the study region was first gridded to 5-km cells, and all MODIS pixels within each cell were determined to contain all oil thickness values (including 0) with different probabilities. A MODIS pixel within the 5-km cell could belong to one of the following five classes (top row in Table 3, plus no data coverage):

T_0 => no oil => thickness t_0= 0 μm

T_1 => thin oil => 0 μm < thickness t_1<1.7 μm (mean = 1)

T_2 => intermediate oil => 1.7 μm < thickness t_2<20 μm (mean = 20)

T_3 => thick oil => 20 μm < thickness t_3 (mean = 50)

T_4 => no observation (due to either no coverage, clouds, land, or sensor artifacts—unlike in the previous method, these were not filled in based on values from nearest neighbors).

Note that the units of $T_{i=0\,\text{to}\,4}$ are percentage cover, with $\sum_{i=0}^{4} T_i = 100\%$. The units of $t_{i=0\,\text{to}\,3}$ are μm.

Downloaded From: https://www.spiedigitallibrary.org/journals/Journal-of-Applied-Remote-Sensing on 16 Mar 2020
Terms of Use: https://www.spiedigitallibrary.org/terms-of-use

Then, the following approach was used to generate T_0, T_1, T_2, T_3, and T_4 for each 5-km cell.

Within each 5-km cell, there are a total of $N_T = 400$ MODIS 250-m pixels. Of these pixels, we have N_j pixels for MODIS class C_j ($j = 0$ to 4, 0: no oil; 1: thin; 2: medium; 3: thick; 4: no observation). Each of these classes will have various percentage cover of $T_{i=0-4}$. Then, the percentage of noncoverage within the 5-km cell is as follows:

$$\mathrm{P}_4 = \mathrm{N}_4/\mathrm{N}_\mathrm{T} \times 100\%. \tag{2}$$

The percentage for each of the $t_{i=0-3}$ classes is as follows:

$$P_{i=0-3} = \left(\sum_{j=0}^{3} T_{i,j} N_j\right) / \sum_{j=0}^{3} N_j x \times 100\%, \tag{3}$$

where $T_{i,j}$ is obtained from Table 3 and subscript j represents the MODIS oil class. To account for nonlinearity during the conversion, $P_{i=0-3}$ is further normalized from 1 to $P4$, resulting in $\sum_{i=0}^{4} P_i = 100$.

This calculation was repeated for each 5-km cell in each image, leading to oil probability distributions for each of the 19 MODIS images.

4.2 *MODIS Classifications and Oil Probability Distributions*

While the complete results of both types of maps (oil classification maps and oil probability maps) can be found in Appendix A5, Figs. 12 and 13 present two examples, one for each type.

Figure 12 shows a MODIS map based on data collected on May 17, 2010. Different oil classes (sheen, thin, and thick) are shown with other categories (no oil, clouds, artifacts, and land). The general distribution is similar to that shown for continuous-scale oil volume maps (Fig. 7) because one was derived from the other. The discrete class map offers a simpler representation. Only a small area near the oil rig was classified as thick oil. As mentioned above, the large area covered by MODIS pixels smears the distribution of patches within each pixel (Fig. 21, Ref. 11).

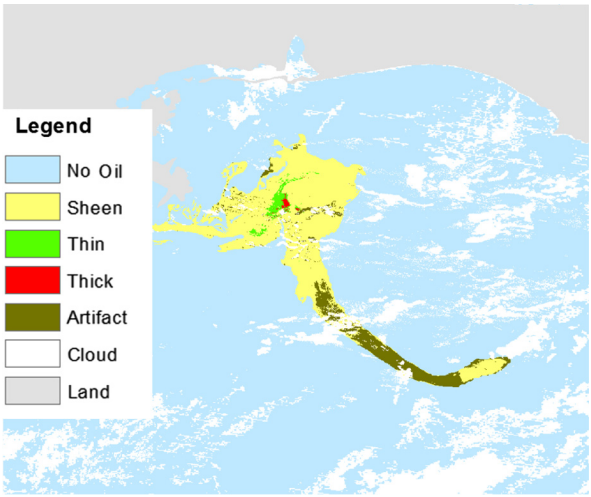


Fig. 12 An example of the MODIS oil thickness classification map for May 17, 2010. This is the same map as in Fig. 7, but the oil volume was classified into different average thicknesses per pixel as defined in Table 2. This map is listed as "product II" in Fig. 3. Sheen: <0.08 μm; thin: 0.08 to 8 μm; thick: >8 μm. The "artifact" in the elongated tail is due to extreme sun glint, where oil thickness estimates are subject to large uncertainties.

Downloaded From: https://www.spiedigitallibrary.org/journals/Journal-of-Applied-Remote-Sensing on 16 Mar 2020
Terms of Use: https://www.spiedigitallibrary.org/terms-of-use

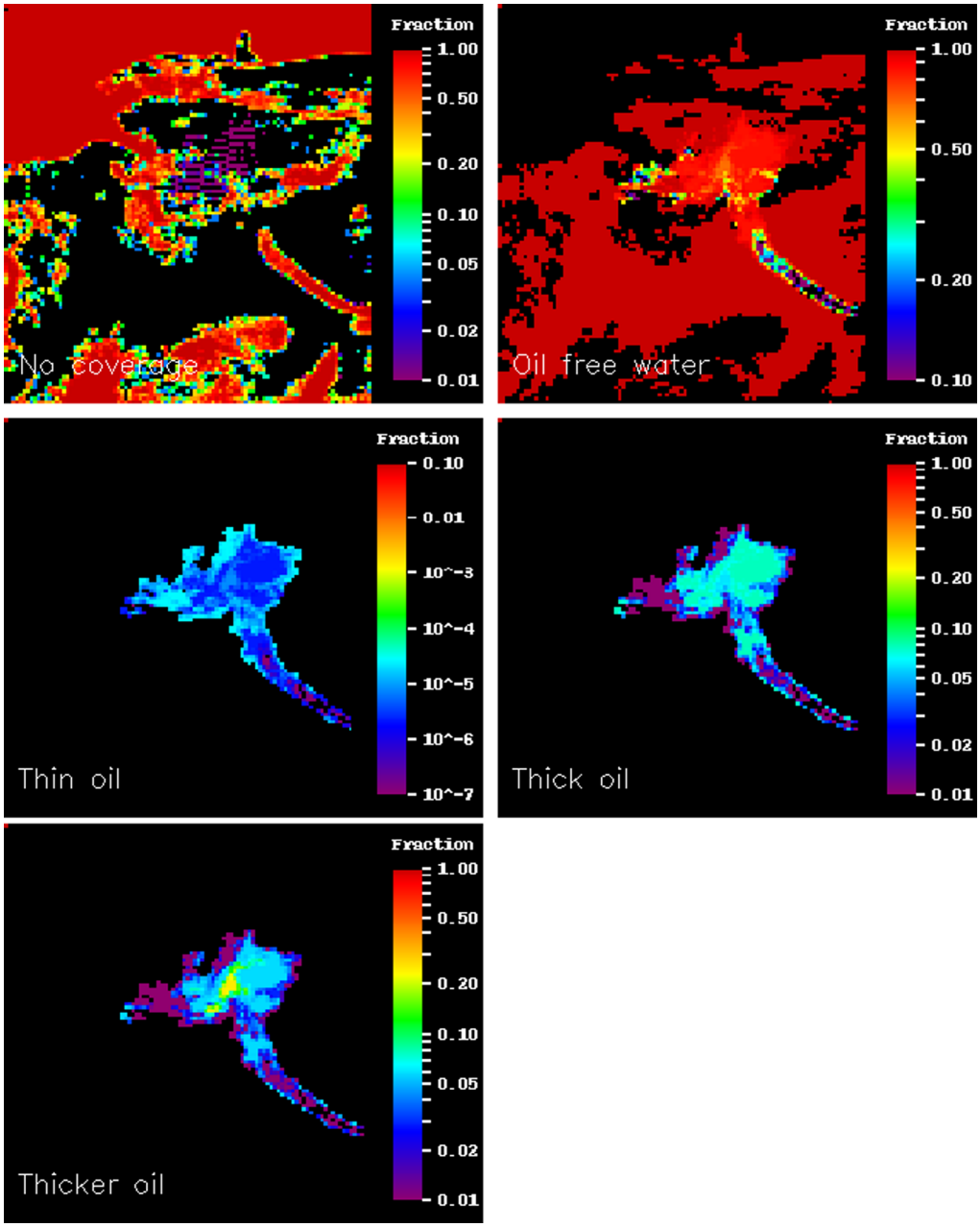


Fig. 13 An example of MODIS oil probability distribution maps for May 17, 2010 (same as in Fig. 12). These maps are listed as "product III" in Fig. 3. The different classes are defined in Table 2: thin: <1.7 μm (mean = 1 μm); thick: 1.7 to 20 μm (mean = 10 μm); thicker: >20 μm (mean = 50 μm). For each 5-km grid cell, the sum probability for all five classes (no observation, oil-free water, thin, thick, and thicker oil) adds up to 1.0. A value of 0.20 in a certain grid cell in the thicker oil class means that 20% of that cell contains thicker oil. Note that because of the large pixel size, most of the pixel is not covered by any oil (i.e., large fractional values in the oil-free water map).

The smearing effect is illustrated in the corresponding MODIS oil probability distribution maps of Fig. 13 for May 17, 2010. Effectively, five maps show the probability values for each of the five classes in each gridded 5-km cell. Other than the "no coverage" class due to land, cloud cover, and other artifacts, the "oil-free-water" class dominates most cells (typically >50%), even within the oil footprint. In other words, over a 25 km^2 area, even within an oil slick area, at least 50% of the surface was not covered by oil. This is likely an artifact derived from the

Downloaded From: https://www.spiedigitallibrary.org/journals/Journal-of-Applied-Remote-Sensing on 16 Mar 2020
Terms of Use: https://www.spiedigitallibrary.org/terms-of-use

AVIRIS-derived oil distribution maps (based on the Tetracorder system), which did not capture oil sheens. As defined here, thick oil (~10 μm) and thicker oil (~50 μm) each covered less than 10% of any given 5-km grid cell, except in the immediate vicinity of the wellhead (Fig. 13). The percent cover for the thin class is nearly zero in all grid cells (<0.01%). This is against the common sense that the majority of the area of oil slick is thin oil.[56] However, as noted previously, the AVIRIS classification that used to calibrate the MODIS observations did not include oil sheen, causing an underestimate in the MODIS-based thin oil class. Similar findings were obtained for all 19 MODIS cases in this study. This underestimation of thin oil coverage does not affect the other two classes (thick and thicker) that are the typical target for oil spill response.

5 Validation

5.1 *Validation Data and Methods*

There are several fundamental difficulties in estimating oil thickness with remote sensing. Specifically, (1) surface oil is very patchy (at the submeter to meter scale) (Fig. 21; Ref. 11), causing mixed pixels in satellite imagery, (2) it is extremely difficult to measure the surface oil thickness (or volume) in the field[17] mainly because it is difficult to collect oil from a known water area, and (3) as a result of 1 and 2, there is no field ground truth data to help calibrate or validate remote sensing observations. Most reliable measurements of oil thickness have been obtained in well-controlled laboratory environments. It is not clear yet how to determine the surface oil thickness, considering waves, a moving boat, or how to correlate it with concurrent reflectance measurements in a heterogeneous environment (see review by Ref. 18). This is a typical problem in oil spill remote sensing research, and, to our best knowledge, none of the published oil spill remote sensing papers has been validated using field measured oil thickness or volume simply because such a field measurement was not possible. Then, without a direct field validation, how much can these coarse-resolution MODIS estimates be trusted?

There are several indirect ways to validate the MODIS-derived oil volume maps. The first is an intuitive evaluation. In the NIR and SWIR wavelengths, increased oil volume, especially with weathered oil, would cause increased backscattering (b_b, m^{-1}) and, to a lesser extent, increased absorption (a, m^{-1}). Because reflectance is roughly proportional to b_b/a, increased oil volume, when oil is emulsified, should lead to increased reflectance in the NIR and SWIR wavelengths. This is actually the concept behind the correlation between MODIS R_{rc} and AVIRIS-derived oil volume.

The second is a qualitative assessment of the MODIS-derived total oil volume on the surface. With oil continuously reached the ocean surface for nearly 3 months, sequential images particularly during the initial spill period should show increased surface oil volume over a gradually larger oil footprint.

Finally, other observations provide independent evaluation of MODIS-derived maps. These observations include satellite-based SAR and airborne photos taken during the course of the blowout event. The details on SAR data processing can be found in Ref. 5. The aerial photographs used to compare with the MODIS oil classification maps are briefly described here.

Over 1600 aerial digital images were retrieved from the NOAA database of DWH photographs, the Environmental Response Management Application (ERMA, 2015) and Ocean Imaging Corporation's archive. From these, 1542 photos were visually compared to MODIS-derived classifications generated for May 9, May 17, June 10, June 26, and July 12, 2010. Each photo contained a GPS-generated latitude, longitude stamp, which was used to geolocate the photograph in ESRI's ArcGIS ArcMap GIS display software. After close visual inspection of the photographs, each was digitally laid over the MODIS oil footprint for the corresponding date. Thus, 816 of the 1542 were selected for categorization and comparison to the MODIS oil thickness classifications. A total of 726 photographs were not suitable for comparison because:

Downloaded From: https://www.spiedigitallibrary.org/journals/Journal-of-Applied-Remote-Sensing on 16 Mar 2020
Terms of Use: https://www.spiedigitallibrary.org/terms-of-use

- they were not within the MODIS product footprint for the matching day;
- the photograph was taken too close to the ocean's surface to be able to discern sufficient spatial information on oil coverage;
- the photograph was taken at a highly oblique angle making the geolocation of the center point of the image misleading in relation to the information in the photograph; or
- the analyst was not able to determine the oil type/thickness in the photograph.

The photographs selected were then grouped into five classes:

- Thick: a significant portion of the photo (~20% or more) contained thick oil;
- Thin: no portion contained thick oil, but a significant portion of the photo (~20% or more) portion contained thin oil;
- Sheen: no portion contained thick or thin oil, but a significant portion of the photo (~20% or more) portion contained oil sheen;
- Nonoil: none of the above was found from the photo.

The ArcGIS class code for the MODIS-derived oil thicknesses was then extracted from the location of each photograph for each date. The results were tabularized into a comparison matrix, as defined by Congalton and Green,[57] Congalton,[58] and Story and Congalton.[59] The photographs were the "reference data." These matrices provide the overall photograph-to-MODIS class accuracy assessment as well as a representation of errors of omission and errors of commission.

Omission errors were calculated by dividing the total number of correctly classified sample units in a category by the total number of sample units in that category from the reference data (the column total). This measure is also called the "producer's accuracy," because from this measurement, the producer of the classification will know how well a certain area was classified.

Commission errors were calculated by dividing the number of correctly classified sample units for a category by the total number of sample units that were classified in that category. This measure is the "user's accuracy," indicating for the user of the map the probability that a sample unit classified on the map actually represents that category on the ground. A Congalton matrix was generated for each of the 5 MODIS days.

5.2 *Validation Results*

5.2.1 *Visual inspection and comparison with oil area*

Each of the MODIS oil products (continuous oil volume maps, oil classification maps, and oil volume probability maps) was visually inspected and compared with the corresponding MODIS RGB images and SWIR R_{rc} data. In each case, high-volume pixels (equivalent to high thickness pixels) corresponded to higher R_{rc} values as compared with lower-volume pixels, regardless of the presence of sun glint. This is expected, as all MODIS products were ultimately derived from R_{rc} data.

Integration of all oil pixels in Fig. 7(b) yields a total volume of about 146 K barrels of oil on May 17, 2010. This is within the volume range estimate from a USGS report (Ref. 60). This volume also represents about 10% of the total estimated oil spilled between April 22 and May 17, assuming a constant spill rate of about 60 K barrels per day.[3]

Much of the spilled oil has been reported to remain in subsurface waters (Ref. 7; references therein). Some of the oil evaporated, although the exact amount is unknown. McNutt et al.[3] reviewed other losses of oil. The MODIS estimates based on AVIRIS-derived oil volume may also be an underestimate, because the Tetracorder spectral shape matching system only mapped thick oil slicks that cause enhanced reflectance in the NIR and SWIR. Most thinner oil slicks were not considered during the USGS analysis, because these thinner slicks lack diagnostic spectral features in the SWIR region.

A temporal consistency check was also used to examine the validity of the results. During the first weeks of the oil spill (April 22 to about mid-May 2010) when mitigation effort (physical removal, burning, use of dispersant) was less intense than in subsequent weeks, surface oil

Downloaded From: https://www.spiedigitallibrary.org/journals/Journal-of-Applied-Remote-Sensing on 16 Mar 2020
Terms of Use: https://www.spiedigitallibrary.org/terms-of-use

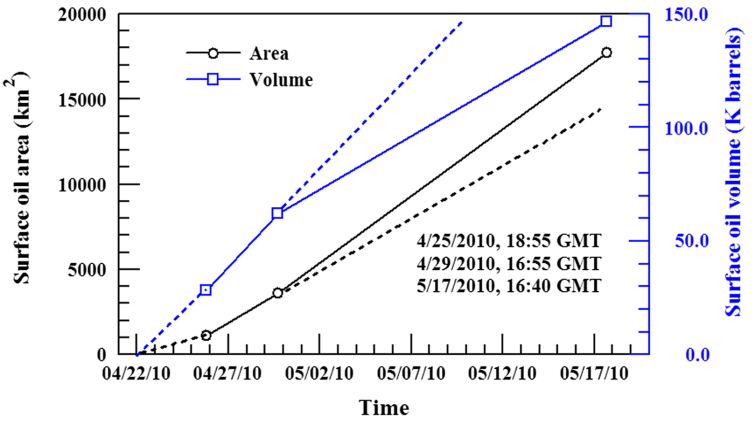


Fig. 14 Surface oil area and volume derived from MODIS measurements on three days. The dotted lines after April 29, 2010, represent linear extrapolation from the April 25, 2010, and April 29, 2010, measurements. On May 17, 2010, the extrapolated oil area is lower than the MODIS estimates, but the extrapolated oil volume is higher than the MODIS estimates, suggesting that the surface oil on May 17, 2010 spread out over a larger area with a lower mean thickness relative to earlier dates.

volume should have increased monotonically. Our results showed that both surface area covered with oil and oil volume on the surface increased from April 25 to May 17 (Fig. 14). This rate of volume increase is lower than that of the area increase after April 29, suggesting that as oil spread widely over time, oil thickness decreased.

5.2.2 *Comparison with concurrent satellite-based SAR measurements*

Garcia-Pineda et al.[5] show that the surface oil footprints derived from nearly concurrent MODIS and satellite-based SAR measurements collected over the GoM during the DWH blowout are very similar. The cumulative oil footprint from the two observation methods was also similar.[5,29] Garcia-Pineda et al.[5] showed that within the SAR-derived oil footprint, bright features match the thick-oil features identified in MODIS imagery. SAR is only considered to differentiate primarily highly emulsified thick oil patches within the oil footprint. Thus, some of the thick oil detected with MODIS is not visible in the corresponding SAR imagery. The integrated oil volume for MODIS-SAR data pairs showed agreement to within 50% in nearly all cases.[7]

Figure 15 shows an example of MODIS and SAR oil distribution maps derived for May 4, 2010. Specifically, an Aqua image was taken at 18:45 GMT and a Cosmo-SkyMED3 (X-Band) image was collected at 23:57 GMT. There is a slight mismatch between the oil footprints from the two measurements, which illustrates the distance that surface oil can travel due to advection and wind-related motion between the two measurement times. Overall, if the SAR and MODIS images are compared side by side, one can see that the separate oil footprint patterns agree well. Similar results were obtained for each of the 19 MODIS images collected within hours of SAR observations. Relatively, bright pixels in the SAR oil footprint that match thick oil slick classes in MODIS represent further evidence that, indeed, these satellite instruments observe different oil thickness.

5.2.3 *Comparison with concurrent airborne photograph interpretations*

Figure 16 provides an example of the comparison between MODIS and aerial photographs, while Table 4 lists the summary statistics of the Congalton matrix, and several representative photos for the different oil classes are presented in Fig. 16. The example shows general agreement in the spatial distributions of various oil classes between MODIS and aerial photographs.

The Congalton matrix results showed a high-degree of mismatches between the sheen and thin classes observed with MODIS and airborne observations. However, there was high fidelity

Downloaded From: https://www.spiedigitallibrary.org/journals/Journal-of-Applied-Remote-Sensing on 16 Mar 2020
Terms of Use: https://www.spiedigitallibrary.org/terms-of-use

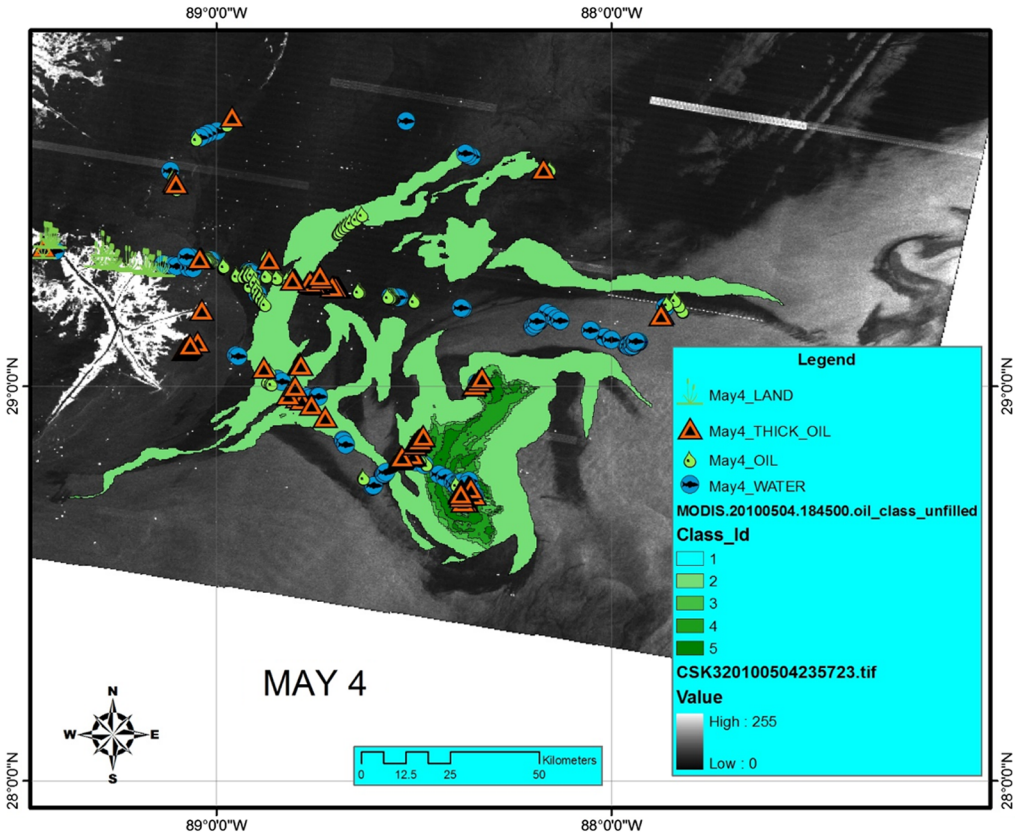


Fig. 15 Comparison between the MODIS-derived oil thickness map and a satellite-derived SAR oil footprint map on May 4, 2010. The SAR image is shown as a gray-scale image in the background. MODIS classes 3, 4, and 5 correspond to thin, thick, and thickest oil, respectively. The location of aerial photographs collected on the same day that show evidence of oil is overlaid on the image (see symbols in the image legend). The displacement in the spatial patterns is due to the nearly 5 h difference in the time of acquisition of the images, which allowed for advection of oil and water (see text).

in the detection of the MODIS thick oil and nonoil classes. This may be due to (1) the underestimate in the MODIS sheen class (i.e., Tetracorder did not map for the presence of sheen oil from AVIRIS), (2) different definitions between MODIS and aerial photographs for the oil classes, (3) a mismatch between the locations of the aerial photo and MODIS pixels, or (4) poor location information associated with a photograph, which typically was shot out of the window of an airplane without sophisticated navigation information to locate the image center on the ground. Given all these difficulties in defining, in particular, the thin oil classes, and inherent differences between the two observations, the overall accuracy of 46% is reasonable. Indeed, if all oil classes were to be combined to have a binary classification (oil and nonoil), the overall accuracy would be much higher, with a producer's accuracy of 94.87% and user's accuracy of 64.35%.

Another way to interpret the accuracy assessment is through the probability distribution maps (Fig. 13). If a MODIS thick oil class (>8 μm) has only 20% of oil cover (80% nonoil) and only 5% in the "thicker" class (50 μm), then, when 100 photos were taken randomly across the MODIS pixel, the likelihood of capturing "thicker" oil would be very small, partially explaining the relatively low accuracy number in Fig. 16 and Table 4.

Abundant airborne photos were taken in four other MODIS days: May 17, June 10, June 26, and July 12. The same visual inspection was conducted to evaluate each MODIS classification, with similar results to those in Table 4, i.e., the accuracy for the sheen and thin classes was lower than for the other classes. The overall accuracy for all these cases generally ranged between 30% and 50%.

In summary, all indirect measures suggest that MODIS can provide useful maps of the total integrated oil volume and spatial distributions of oil thickness. Their absolute accuracy cannot be

Downloaded From: https://www.spiedigitallibrary.org/journals/Journal-of-Applied-Remote-Sensing on 16 Mar 2020
Terms of Use: https://www.spiedigitallibrary.org/terms-of-use

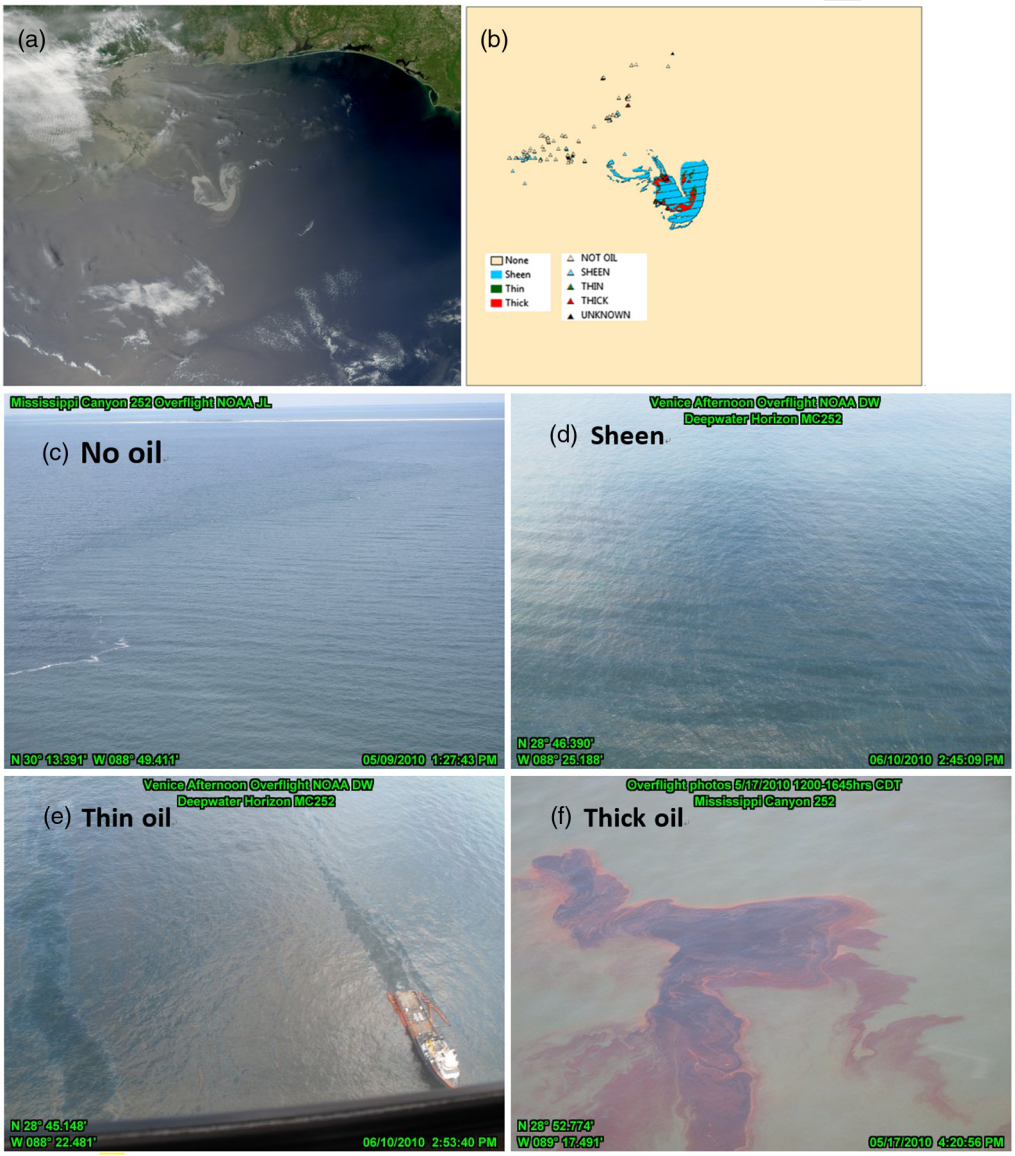


Fig. 16 (a) and (b) Comparison between MODIS classified oil map on May 9, 2010, and airborne photo classification results (triangles). Each of the 193 photos was visually inspected and interpreted independently from the MODIS observations to contain oil of different classes (including nonoil). The statistics for this comparison are listed in Table 4. (c)–(f) Sample photos for the four classes (not oil, sheen, thin, and thick) are provided.

directly verified due to lack of concurrent field data. Even if there were accurate and concurrent field measurements of slick thickness, it would still be very challenging to compare with the large MODIS pixel. Indeed, this is one primary reason why MODIS classification maps and probability maps were derived from the continuous oil maps, as the former would provide oil distributions on a relative sense (thin, medium, and thick) rather than absolute values while the latter would provide the probability of encountering oil of different thicknesses at a given location.

6 Discussion: Uncertainties, Strengths, and Weaknesses

The empirical approach used here for estimating oil volume over synoptic scales based on optical satellite imagery relies on a transfer function that applies results derived empirically from one instrument (AVIRIS) to another (MODIS). Our analysis was based on AVIRIS/Tetracorder-

Downloaded From: https://www.spiedigitallibrary.org/journals/Journal-of-Applied-Remote-Sensing on 16 Mar 2020
Terms of Use: https://www.spiedigitallibrary.org/terms-of-use

Table 4 Evaluation of the MODIS oil thickness classification map on May 9, 2010, using 193 airborne photos. For each cross examination between MODIS classes and photo classes, producer's accuracy and user's accuracy are calculated. If the photos were used as the "truth" (most of them were taken under "not oil" condition), the overall accuracy of the MODIS classification is 46.11%, while the accuracy of each class varies. These results are corresponding to Fig. 16.

	Reference data				
	Photo thick oil	Photo thin oil	Photo sheen	Photo not oil	Total
MODIS thick oil	13	32	1	1	47
MODIS thin oil	2	1	0	0	3
MODIS sheen oil	10	14	1	3	28
MODIS not oil	16	5	20	74	115
Total	41	52	22	78	193

Producer's accuracy	User's accuracy	Overall accuracy
Thick oil = 31.71%	Thick oil = 27.66%	Total accurate = 89
Thin oil = 1.92%	Thin oil = 33.33%	Overall accuracy = 89/193 = 46.11%
Sheen oil = 4.55%	Sheen = 3.57%	
Not oil = 74/78 = 94.87%	Not oil = 74/115 = 64.35%	
Total photos viewed: 314		
Not used: duplicate: 0		
Not used: undeterminable: 120		
Not used: out of MODIS foot print: 1		

derived oil volume distributions on a single day (May 17, 2010). Any uncertainties associated with such a limited analysis would be carried over to the MODIS products. In our estimation, the MODIS-derived distributions are underestimates of the total oil found on the sea surface during the DWH event. They may be interpreted as relative patterns even though the absolute values were provided.

We conducted limited validations of presence of oil on the surface based on information provided by observers on the ground and from aircraft photography. Yet, there is still no concurrent, direct measurements of oil thickness to validate the results from coarse-resolution remote sensing. Although the technical approach may not be ideal, we used the best data available. The histogram matching approach provided results that are consistent with other datasets and estimates derived independently from other remote sensing data.

We are not aware of any use of field-measured oil thickness in validating remote sensing estimates in any published paper. Developing field methods for quantifying oil slicks represents one of the immediate needs in oil spill remote sensing research. On the other hand, even in carefully controlled laboratory conditions, oil thickness can vary by orders of magnitude over minimal spatial scales.[61] In our study, it was clear that oil thickness across a 250-m pixel is not uniform. AVIRIS data show patchy oil at subpixel scales (Fig. 21; Ref. 11). These patches change the MODIS R_{rc} and our estimates are thus approximations. Again, the aim of this approach was to identify areas of relatively thick oil to understand their distribution at the surface over synoptic scales to guide oil spill response, rather than to ascertain the volume and subpixel distribution of oil with a high degree of uncertainty.

The three-thickness classes for MODIS were based on AVIRIS statistics (Appendix A4, Fig. 22). More thickness classes could certainly be defined, yet they perhaps would not yield more information since absolute oil thickness could not be validated directly. A sensitivity analysis showed that even after the MODIS oil maps were divided into five classes instead of three, the resulting oil probability maps are similar (Table 1).

Downloaded From: https://www.spiedigitallibrary.org/journals/Journal-of-Applied-Remote-Sensing on 16 Mar 2020
Terms of Use: https://www.spiedigitallibrary.org/terms-of-use

A significant limitation in oil volume assessment over synoptic scales such as required to evaluate the entire GoM was spatial resolution. Finer-spatial resolution sensors such as Landsat (30-m) did not cover the spill—in part because of its narrow swath (~180 km) and in part because of its infrequent revisit time of 8 days with two sensors in orbit. The Sentinel-2 sensors may provide revisit times of 5 days with two sensors flying simultaneously, each with a separate set of viewing geometries. Until a new type of sensor with fine spatial-resolution and wide swath is put in orbit, this problem has to be addressed through multisensor data fusion, such as done here with two separate MODIS sensors.

During the DWH oil spill, MODIS-based surface-oil distribution maps were generated in near real-time to share with stakeholders.[29] The maps showed presence or absence of oil on the ocean surface without information on oil volume. Empirical approaches such as the one demonstrated here may provide additional useful information on the relative distribution patterns of oil of different thicknesses. This is true even when AVIRIS or similar hyperspectral measurements are not available to provide oil volume estimates to scale MODIS reflectance data. In such cases, the conceptual relationship between MODIS R_{rc} and oil volume (per MODIS pixel; Fig. 5) may still be used to classify oil thickness for each oil-containing pixel, although the thresholds to separate different classes need to be verified.

Eventually, it would be ideal if thickness estimates could be derived from optical models based on radiative transfer theory, optical properties of oil and water, and field observations of oil on the surface of aquatic environments under different conditions (wind speed and direction, sun and viewing angles, etc). Ideally, imaging spectrometer data collected over large swath widths, at fine spatial resolution, and with frequent revisit times should be used in concert with other remote sensing data, including SAR, to overcome many of the limitations inherent in any one technology to quantitatively map oil spills.

7 Conclusions

Fine-resolution hyperspectral airborne measurements provide important information about the spatial distribution of different types of oil emulsions that can be used to scale up rough estimates of oil thickness to map oil distribution over synoptic spatial scales with coarse-resolution satellite measurements. These observations help to develop surface oil volume distributions maps. The combination of methods helps to derive relative oil thickness classes and oil probability maps. Although they may contain large degree of uncertainties, as no method was available to measure oil thickness in the field to validate these estimates, these approaches represent a step forward toward the ultimate goal of identifying areas of thick (actionable) oil using readily available satellite data. Such remotely sensed oil distribution maps may also help assess a spill's potential impacts to the marine environment. These approaches may thus be used in future spills to provide rapid assessment of thin and thicker oils on the ocean surface in order to help response efforts in near real-time and postspill assessment retrospectively. The study also shows the advantage of using optical remote sensing data to estimate not only the oil spill footprint but also the surface oil volume as long as data of sufficient spectral and spatial resolutions are available.

Appendix A

A1 Cloud Masking for MODIS Sun Glint Imagery Over Oil Spill

Existing cloud masking methods were not designed for differentiating clouds from oil under sun glint, and they often treat oil slicks as clouds. A new cloud masking method was developed to address the issue.

The cloud masking uses a region-based modeled texture analysis, where image subsets are modeled as being comprised of noise and a number of subelements each with its own texture. A parametric, generative model then recreates the observed intensity through a probability distribution function (PDF). The PDF is formed from a combination of functions representing the image's known structural information.

Downloaded From: https://www.spiedigitallibrary.org/journals/Journal-of-Applied-Remote-Sensing on 16 Mar 2020
Terms of Use: https://www.spiedigitallibrary.org/terms-of-use

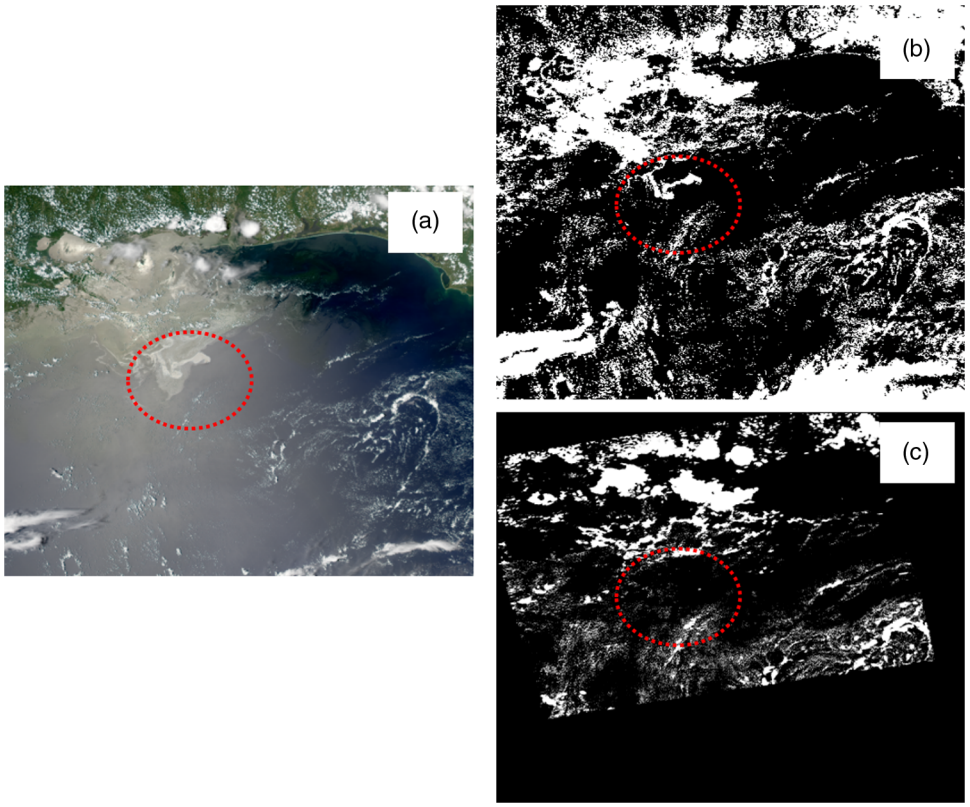


Fig. 17 (a) MODIS RGB image on June 26, 2010, shows oil slicks in the northern GoM; (b) standard MOD35 cloud mask falsely interprets thick oil as clouds; and (c) PDF cloud mask avoids this problem.

Images for analysis are generated from the ratio of MODIS bands 1 and 2 (B1 = 645 nm and B2 = 859 nm). Image preprocessing involves subsetting the image for the area of interest and flattening to remove the large-scale gradient. Flattened images exhibit ~10% large-scale variations, whereas unflattened images vary by factors of 3 to 5. The PDF rolling window is run through such preprocessed images, where fine-scale structure is retrieved by advancing the window by one or two pixels.

Although a straight threshold approach could be applied to identify clouds, detailed investigation of spill image subsets reveals significant intensity overlap between small dark clouds and their shadows, water, and thin oil in the intensity-flattened image. The PDF texture analysis models the PDF to partition scene elements rather than intensity thresholding, where the model parameters are tuned for each image to obtain the best results from visual inspection.

Figure 17 shows a comparison between the MODIS standard cloud mask (MOD35) and the new PDF cloud mask. The MOD35 cloud mask falsely interprets thick oil as clouds, whereas the PDF cloud mask avoids this problem. For all 19 MODIS images, the PDF method showed much improved cloud masks. The small artifacts (false positive and false negative) from the PDF cloud masks were manually corrected. The end products were applied to all MODIS oil products to mask cloud pixels. In calculating statistics, these pixels were treated as no data.

A2 Why a Histogram Matching Method was Chosen

Our first attempt in correlating AVIRIS with MODIS was to extract spectral data from the corresponding pixels along an artificial transect line, as shown in Fig. 18(a). Along this line, several AVIRIS pixels were visually chosen to represent thick oil, thin oil, and oil-free water,

Downloaded From: https://www.spiedigitallibrary.org/journals/Journal-of-Applied-Remote-Sensing on 16 Mar 2020
Terms of Use: https://www.spiedigitallibrary.org/terms-of-use

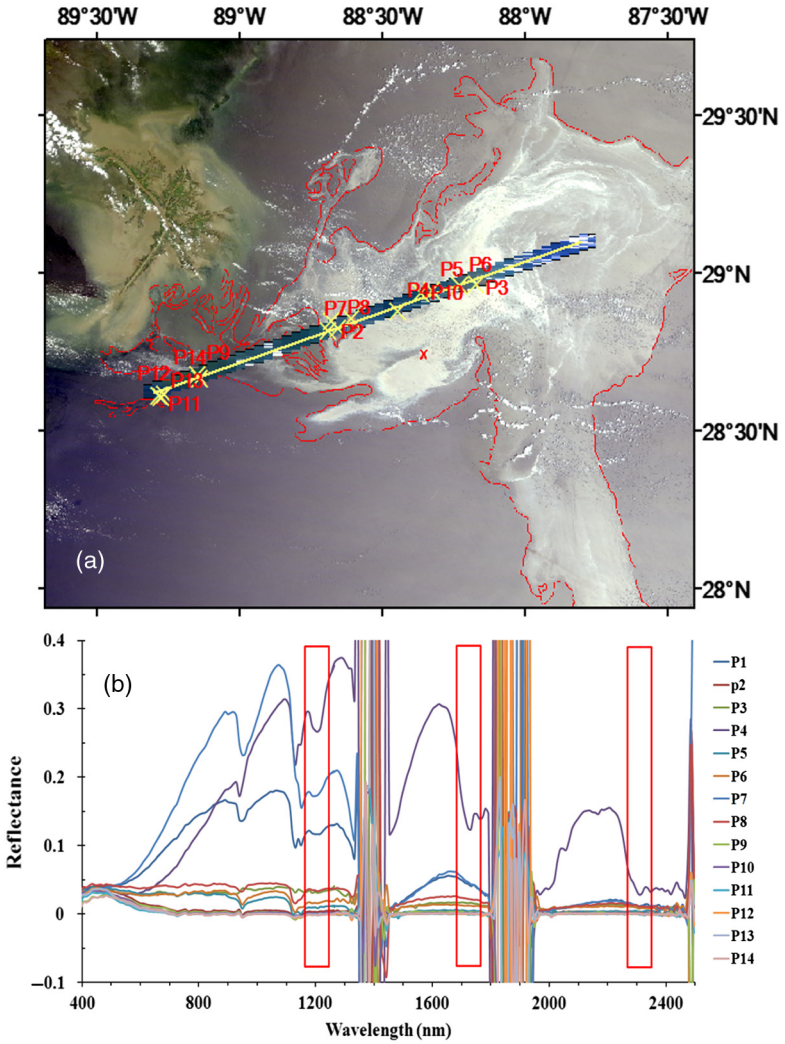


Fig. 18 (a) MODIS RGB image on May 17, 2010, showing the surface oil slicks outlined in red. Overlaid is one AVIRIS flight line (run 10) on the same day, with 14 points annotated, where reflectance spectra are extracted and shown in (b). The red X marks the location of the DWH oil spill site. The vertical rectangular boxes mark the spectral curvatures around 1.2, 1.73, and 2.3 μm that are used by the USGS[12] to determine the oil/water mixing ratio and thick oil volume per area.

where their reflectance spectra are shown in Fig. 18(b). Compared with oil-free water pixels whose reflectances in the NIR and SWIR are near zero, both thick and thin oil pixels showed elevated reflectances in these spectral ranges. Only thick oil pixels showed spectral curvatures around 1.2, 1.7, and 2.3 μm, where Clark et al.[12] algorithm could be used to derive the oil thickness and volume. This spectral continuum removed absorption depth increases with increasing thickness of an emulsion slick.

Figure 19 shows R_{rc} spectra of three MODIS pixels over oil-free water, thin oil, and thick oil. For each MODIS pixel, the corresponding mean and standard deviation of AVIRIS spectra (extracted within the footprint of the MODIS pixel) are also shown in the figure in order to determine whether there is any relationship between MODIS and AVIRIS reflectance. The results in Fig. 19 indicate that although the water pixels showed the lowest reflectance for both MODIS and AVIRIS, it is difficult to generalize any rules to relate MODIS and AVIRIS reflectances or reflectance ratios. This is because nearly all MODIS pixels contained significant sun glint, which not only increased MODIS R_{rc} in all bands but also changed the R_{rc} spectral shape. By contrast, sun glint effects were

Downloaded From: https://www.spiedigitallibrary.org/journals/Journal-of-Applied-Remote-Sensing on 16 Mar 2020
Terms of Use: https://www.spiedigitallibrary.org/terms-of-use

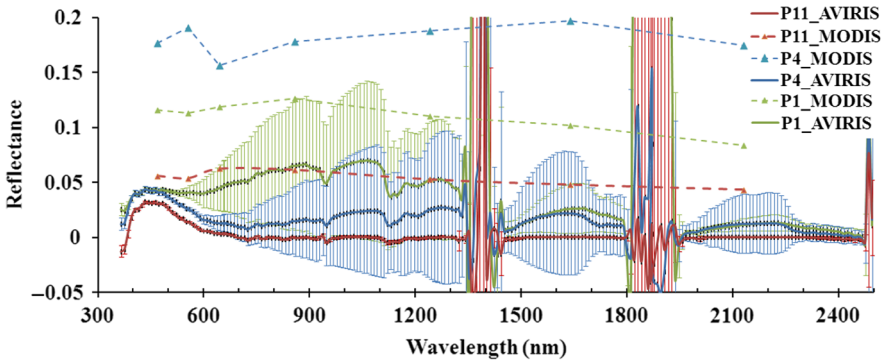


Fig. 19 R_{rc} spectra from three MODIS pixels [P1, P4, P11, locations annotated in Fig. 18(a)], with corresponding AVIRIS surface reflectance averages and their standard deviations overlaid. One MODIS pixel (250-m resolution) corresponds to about 900 AVIRIS pixels (~7.6-m resolution).

avoided by the AVIRIS measurements. Note that while there is little variation among adjacent AVIRIS pixels for the visible wavelengths (in particular, <500 nm, see small standard deviations in Fig. 19), substantial variations are found among these pixels for longer wavelengths, as indicated by the much higher standard deviations. This is because that thick oil slicks are typically patchy, causing large variations in reflectance among adjacent pixels,[11] for otherwise, the reflectance at long wavelengths (>500 nm) should be persistently small with limited standard deviations due to the high water absorption in these bands.

Figure 19 and other spectral analyses[62] indicated that it is impossible to establish a statistical regression between AVIRIS and MODIS reflectance due to the presence of sun glint. Alternative approaches must be developed to relate the two observations. We then attempted to correlate MODIS reflectance and AVIRIS-derived oil thickness. Figure 20(a) shows MODIS R_{rc}, 555 along the W-E transect and the mean oil thickness corresponding to the MODIS pixels. For each MODIS pixel, only AVIRIS pixels with nonzero thickness were used to calculate the mean. There is a general correlation east of 88.7°W, but the correlation of $R_{rc,555}$, west of this longitude is poor. The result became worse when all AVIRIS pixels were used to calculate the mean oil thickness [Fig. 20(b)], where little correlation was found between MODIS $R_{rc,555}$ and AVIRIS-derived mean oil thickness. This later case applies to potential extrapolation of the correlation of $R_{rc,555}$, 555 between MODIS and AVIRIS data. Thus, pixelwise regression between the two would not lead to reliable estimates from MODIS R_{rc} data. This also led to the conclusion that histogram matching was perhaps the only feasible option.

A3 Heterogeneity of Oil Patches

Even though AVIRIS pixels (7.6-m resolution) show oil slicks thicker than 60 μm, after averaging over a MODIS pixel (250-m resolution), the mean thickness is much reduced. This phenomenon can be viewed from the high standard deviations along the AVIRIS transect line in Fig. 20 and is further illustrated in Fig. 21 below. Oil on the sea surface is typically very patchy, and high-resolution thick-oil pixels will then be smeared by more numerous thinner-oil pixels in lower-spatial resolution images (1 MODIS 250-m pixel corresponds to 900 AVIRIS pixels). The smearing effect can be clearly visualized in Fig. 21, where most of AVIRIS pixels contain thin oil. Although the smearing effect is linear in oil volume, it is nonlinear between reflectance and oil volume, and this is one reason why a histogram-matching method was used in this study to estimate oil volume from MODIS measurements.

More details about the oil slick heterogeneity can be found in Sun et al.[11]

Downloaded From: https://www.spiedigitallibrary.org/journals/Journal-of-Applied-Remote-Sensing on 16 Mar 2020
Terms of Use: https://www.spiedigitallibrary.org/terms-of-use

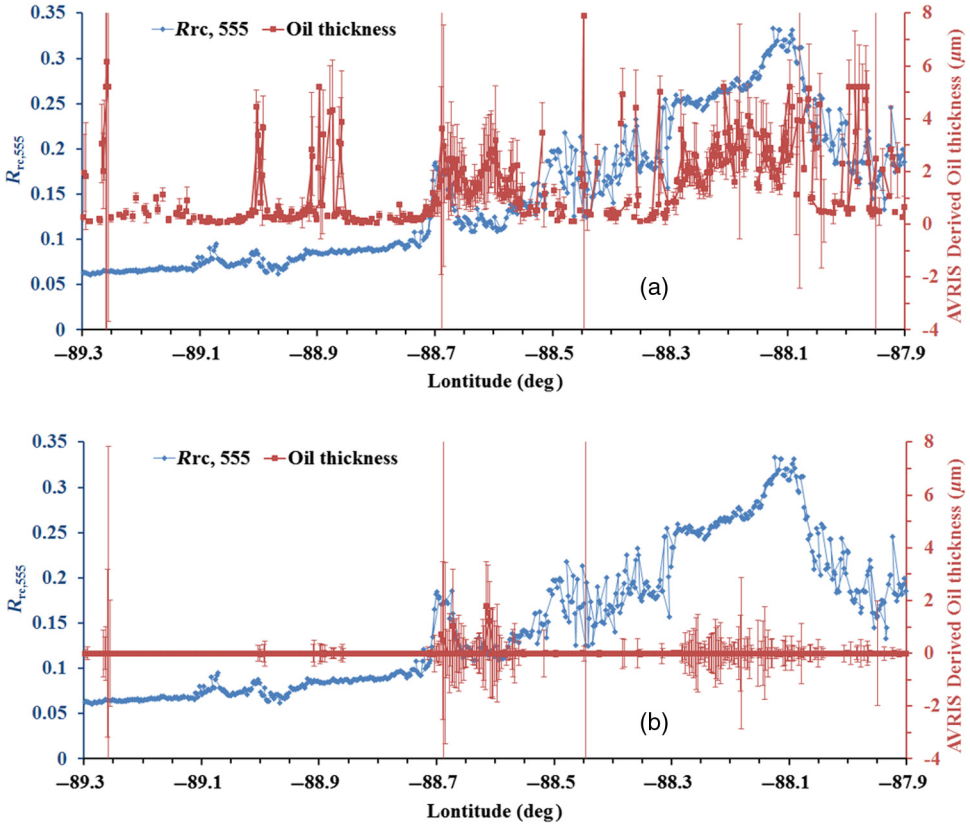


Fig. 20 MODIS reflectance (R_{rc}) at 555 nm and AVIRIS-derived oil thickness along the W-E AVIRIS flight line (run 10) on May 17, 2010 [yellow line in Fig. 18(a)]. For each MODIS pixel along this line, the corresponding AVIRIS pixels were used to calculate the mean and standard deviation of oil thickness (in μm). (a) Only AVIRIS pixels with thickness >0 were used. (b) All noncloud AVIRIS pixels were used. Note that a 250-m MODIS pixel represents the area of over 1000 AVIRIS pixels. When only a small portion of AVIRIS pixels shows thickness >0, the trends in panel (a) tend to be smeared in panel (b) due to the mean calculations.

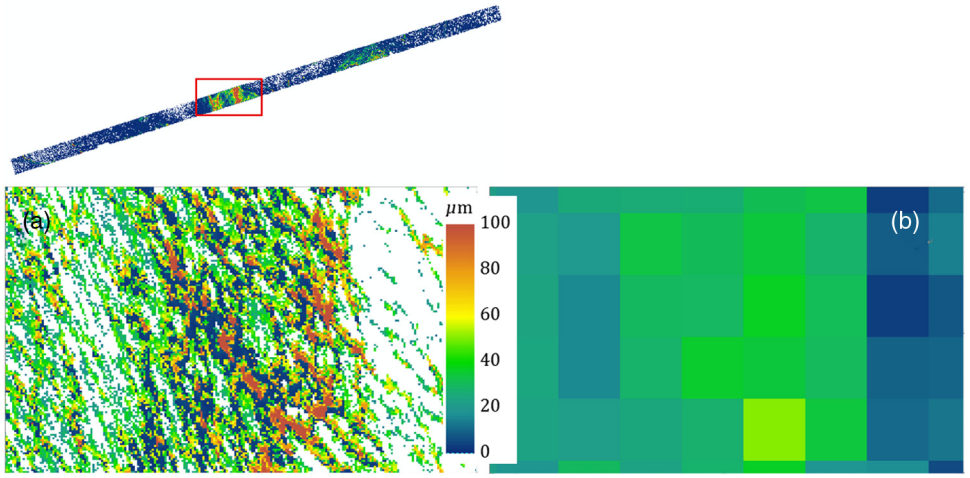


Fig. 21 (a) Oil slicks identified from the AVIRIS flight line (top) on May 17, 2010. They show an oil thickness range of 0 to >100 μm. (b) The corresponding MODIS pixels show much lower range as a result of pixel averaging.

Downloaded From: https://www.spiedigitallibrary.org/journals/Journal-of-Applied-Remote-Sensing on 16 Mar 2020
Terms of Use: https://www.spiedigitallibrary.org/terms-of-use

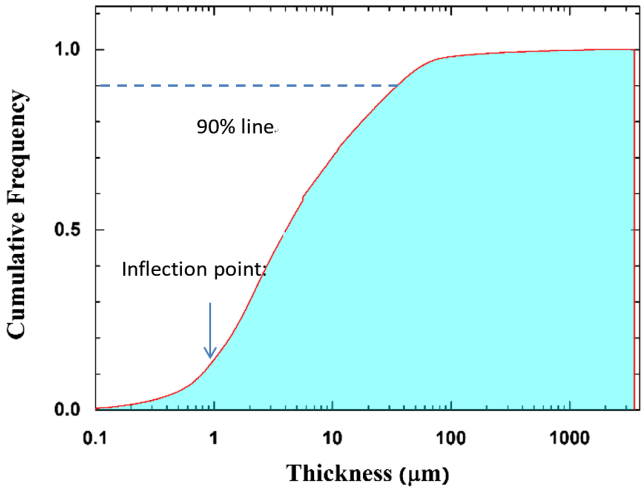


Fig. 22 Estimates of the three-class oil thickness values from AVIRIS statistics. The *x*-axis shows the AVIRIS-derived oil thickness for all oiled pixels shown in Fig. 1(b). The *y*-axis shows the cumulative frequency of these pixels.

A4 Define Oil Thickness Classes Based on BONN Agreement and AVIRIS Statistics

In nature, oil thickness distribution tends to be log normal: most of the oiled pixels have thin oil and fewer pixels contain thicker oil.[56] Then, in converting the ranges in the BONN agreement into mean values, it makes more sense to use geometric mean rather than arithmetic mean. Also, the USGS Tetracorder shape-matching system was used to detect thick oil (emulsions) and was not used to detect oil sheens, as defined in the BONN table. The Tetracorder system, however, calculated the subpixel fractional oil coverage for an "oiled" pixel, resulting in thinner oil calculations when the pixel was considered as a whole. Thus, the mean value corresponding to the range Rainbow (0.30 to 5 μm) is $\text{sqrt}(0.30 \times 5) = 1.2$ μm. If half of the sheen class (>0.15 μm) can be observed by AVIRIS, the mean value is $\text{sqrt}(0.15 \times 5) = 0.87$ μm. Thus, the mean value representing the thin class after taking into account of the Bonn agreement and AVIRIS capacity was taken as 1 μm. This choice can also be seen in the cumulative frequency curve in Fig. 22, where the lower inflection point is about 0.7 μm.

The next class from the Bonn agreement (Metallic, 5.0 to 50 μm) corresponds to $\text{sqrt}(5 \times 50) = 15.8$ μm. The next class (transitional dark, 50 to 200) corresponds to $\text{sqrt}(50 \times 200) = 100$. Then, if the medium and thick classes were to be defined from the BONN agreement, the mean values representing these classes would be 16 and 100 μm, respectively. However, based on AVIRIS observations (8-m resolution), these numbers were adjusted. Figure 22 shows the cumulative frequency distribution of AVIRIS-derived oil thickness for all oiled pixels shown in Fig. 2(b). The 90% line corresponds to about 40 μm. This agrees well with the report by Hollinger and Mennella[56] that 90% of the oil was in 10% of the slick area. As a compromise between this value and the mean value for the BONN agreement (100 μm), the mean thickness for the thick class was then chosen to be 50 μm.

Taking 40 μm as the top thickness of the intermediate class, the mean thickness of the intermediate class is $\text{sqrt}(5 \times 40) \approx 14$ μm. Rounding to the nearest 10 would yield a mean thickness of 10 μm.

When applying these three mean values (1, 10, 50 μm) to AVIRIS data, it was found that the thickness ranges corresponding to these mean values are (>0 but <1.7 μm), (>1.7 but <20 μm), and (>20 μm), respectively. These ranges were used to derive oil probability maps from the MODIS-derive oil thickness classification maps.

A5 MODIS-Derived Surface Oil Maps

For each of the 19 MODIS images, three types of oil distributions maps were derived in this study and provided below for reference (Figs. 23–41). They are: (1) continuous oil volume; (2) oil classifications; and (3) oil probabilities.

Downloaded From: https://www.spiedigitallibrary.org/journals/Journal-of-Applied-Remote-Sensing on 16 Mar 2020
Terms of Use: https://www.spiedigitallibrary.org/terms-of-use

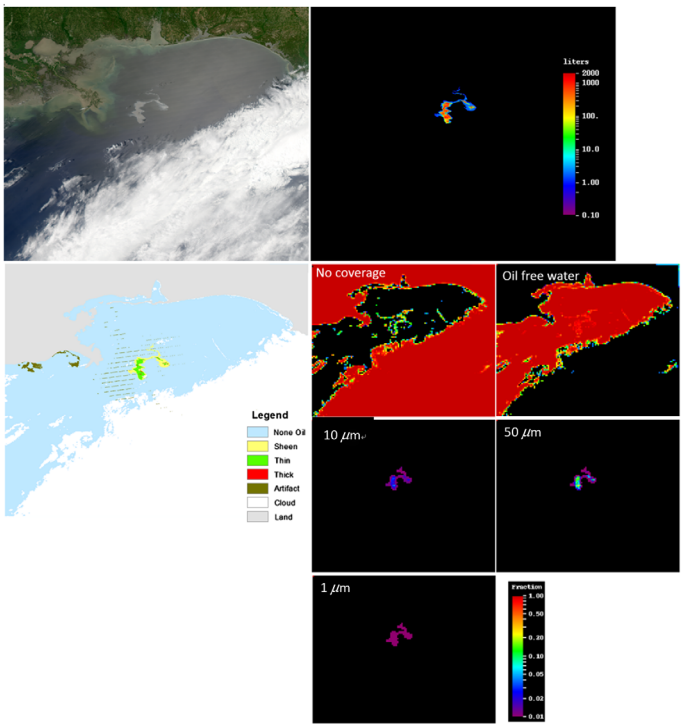


Fig. 23 April 25, 2010, 18:55 GMT. Top left: MODIS RGB image; top right: surface oil volume (liters per MODIS 250-m pixel) ("product I" in Fig. 3); bottom left: surface oil classes (sheen, thin, and thick) ("product II" in Fig. 3); bottom right: surface oil probability (e.g., 0.10 represents that 10% of the surface is covered by the corresponding class) ("product III" in Fig. 3).

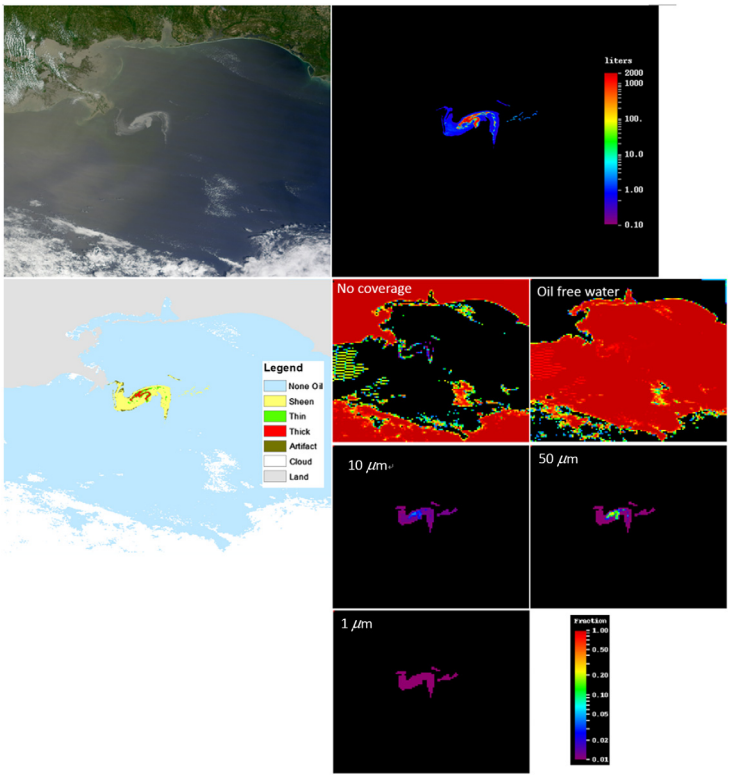


Fig. 24 April 29, 2010, 16:55 GMT. Top left: MODIS RGB image; top right: surface oil volume (liters per MODIS 250-m pixel) ("product I" in Fig. 3); bottom left: surface oil classes (sheen, thin, and thick) ("product II" in Fig. 3); bottom right: surface oil probability (e.g., 0.10 represents that 10% of the surface is covered by the corresponding class) ("product III" in Fig. 3).

Downloaded From: https://www.spiedigitallibrary.org/journals/Journal-of-Applied-Remote-Sensing on 16 Mar 2020
Terms of Use: https://www.spiedigitallibrary.org/terms-of-use

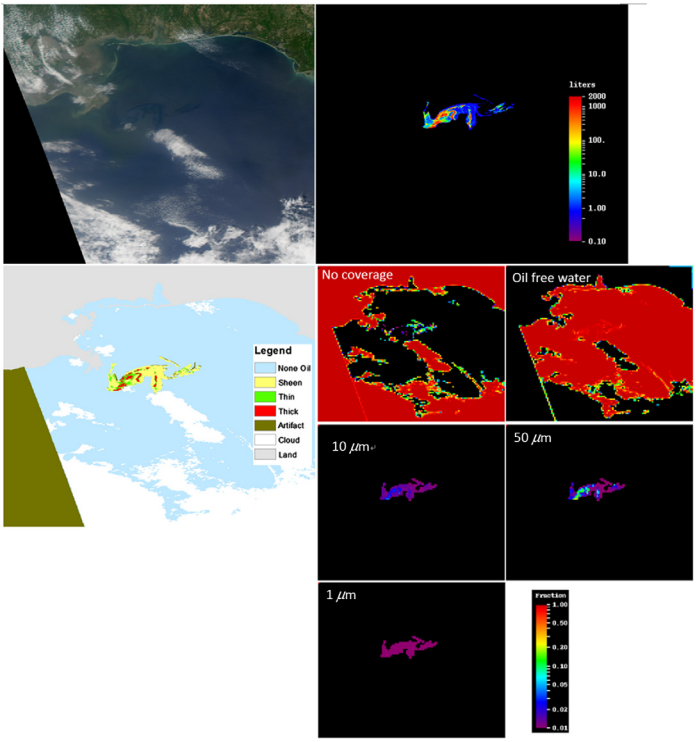


Fig. 25 April 29, 2010, 18:30 GMT. Top left: MODIS RGB image; top right: surface oil volume (liters per MODIS 250-m pixel) ("product I" in Fig. 3); bottom left: surface oil classes (sheen, thin, and thick) ("product II" in Fig. 3); bottom right: surface oil probability (e.g., 0.10 represents that 10% of the surface is covered by the corresponding class) ("product III" in Fig. 3).

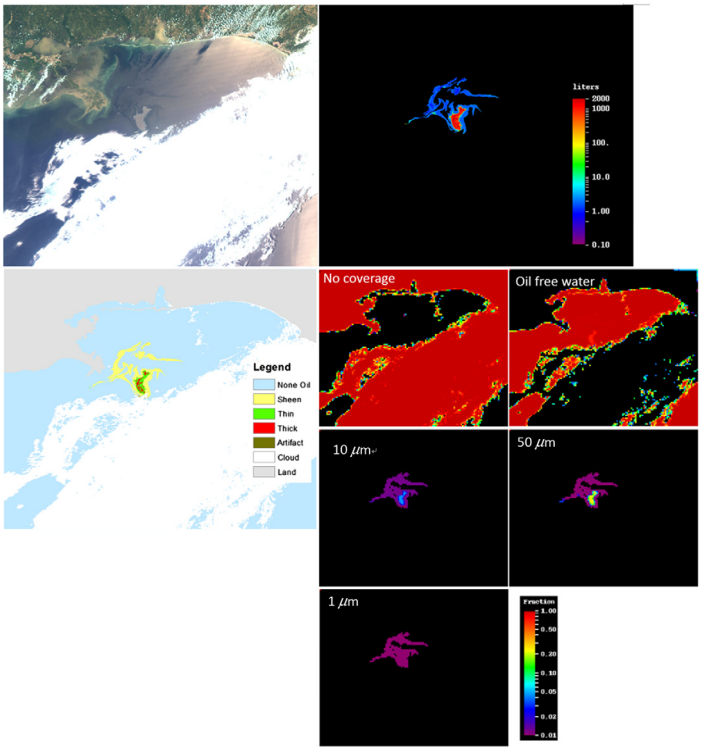


Fig. 26 May 04, 2010, 18:45 GMT. Top left: MODIS RGB image; top right: surface oil volume (liters per MODIS 250-m pixel) ("product I" in Fig. 3); bottom left: surface oil classes (sheen, thin, and thick) ("product I" in Fig. 3); bottom right: surface oil probability (e.g., 0.10 represents that 10% of the surface is covered by the corresponding class) ("product I" in Fig. 3).

Downloaded From: https://www.spiedigitallibrary.org/journals/Journal-of-Applied-Remote-Sensing on 16 Mar 2020
Terms of Use: https://www.spiedigitallibrary.org/terms-of-use

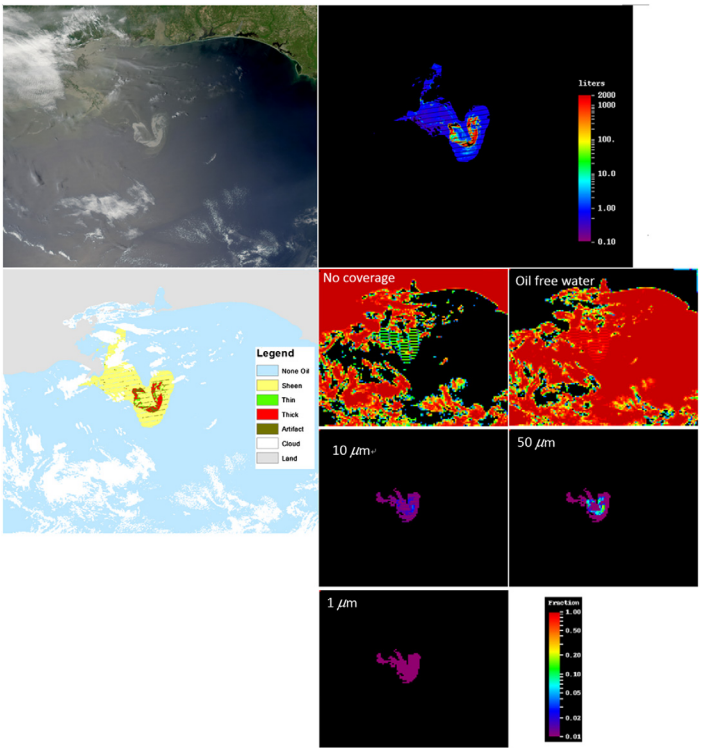


Fig. 27 September 05, 2010, 19:05 GMT. Top left: MODIS RGB image; top right: surface oil volume (liters per MODIS 250-m pixel) ("product I" in Fig. 3); bottom left: surface oil classes (sheen, thin, and thick) ("Product I" in Fig. 3); bottom right: surface oil probability (e.g., 0.10 represents that 10% of the surface is covered by the corresponding class) ("product I" in Fig. 3).

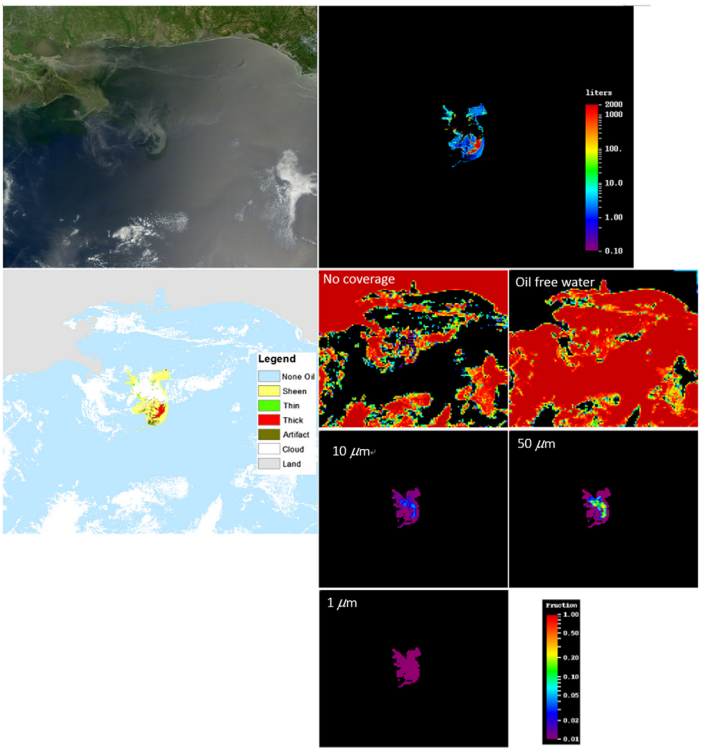


Fig. 28 May 10, 2010, 16:35 GMT. Top left: MODIS RGB image; top right: surface oil volume (liters per MODIS 250-m pixel) ("product I" in Fig. 3); bottom left: surface oil classes (sheen, thin, and thick) ("product I" in Fig. 3); bottom right: surface oil probability (e.g., 0.10 represents that 10% of the surface is covered by the corresponding class) ("product I" in Fig. 3).

Downloaded From: https://www.spiedigitallibrary.org/journals/Journal-of-Applied-Remote-Sensing on 16 Mar 2020
Terms of Use: https://www.spiedigitallibrary.org/terms-of-use

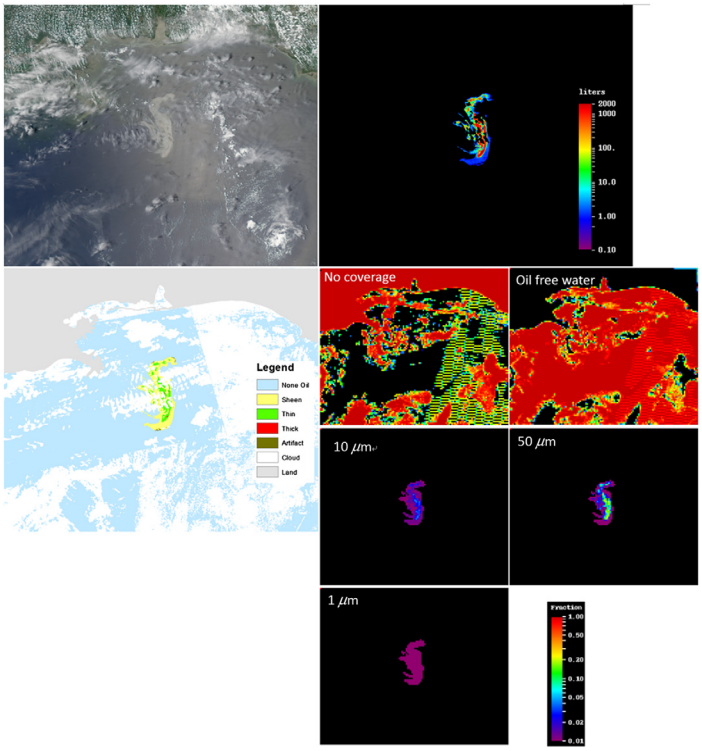


Fig. 29 May 11, 2010, 18:55 GMT. Top left: MODIS RGB image; top right: surface oil volume (liters per MODIS 250-m pixel) ("product I" in Fig. 3); bottom left: surface oil classes (sheen, thin, and thick) ("product I" in Fig. 3); bottom right: surface oil probability (e.g., 0.10 represents that 10% of the surface is covered by the corresponding class) ("product I" in Fig. 3).

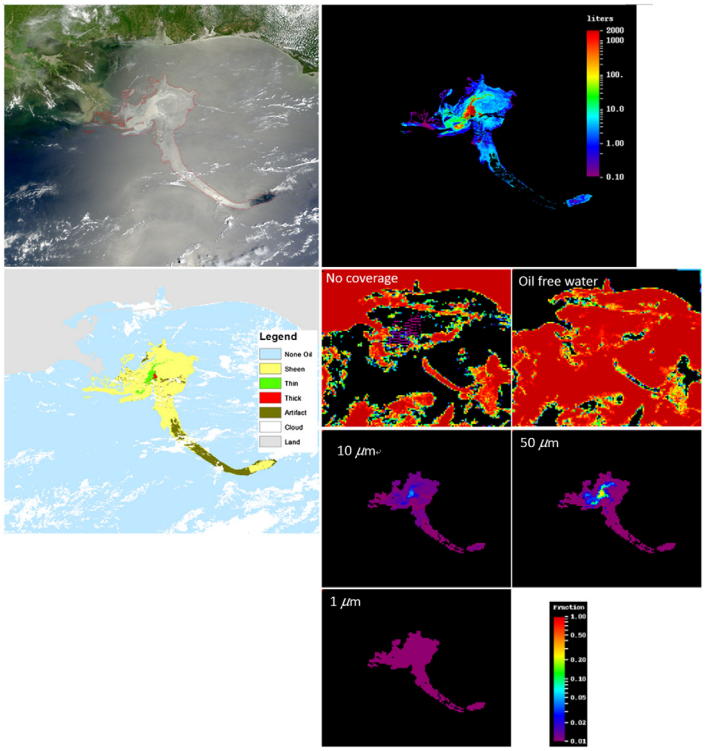


Fig. 30 May 17, 2010, 16:40 GMT. Top left: MODIS RGB image; top right: surface oil volume (liters per MODIS 250-m pixel) ("product I" in Fig. 3); bottom left: surface oil classes (sheen, thin, and thick) ("product I" in Fig. 3); bottom right: surface oil probability (e.g., 0.10 represents that 10% of the surface is covered by the corresponding class) ("product I" in Fig. 3).

Downloaded From: https://www.spiedigitallibrary.org/journals/Journal-of-Applied-Remote-Sensing on 16 Mar 2020
Terms of Use: https://www.spiedigitallibrary.org/terms-of-use

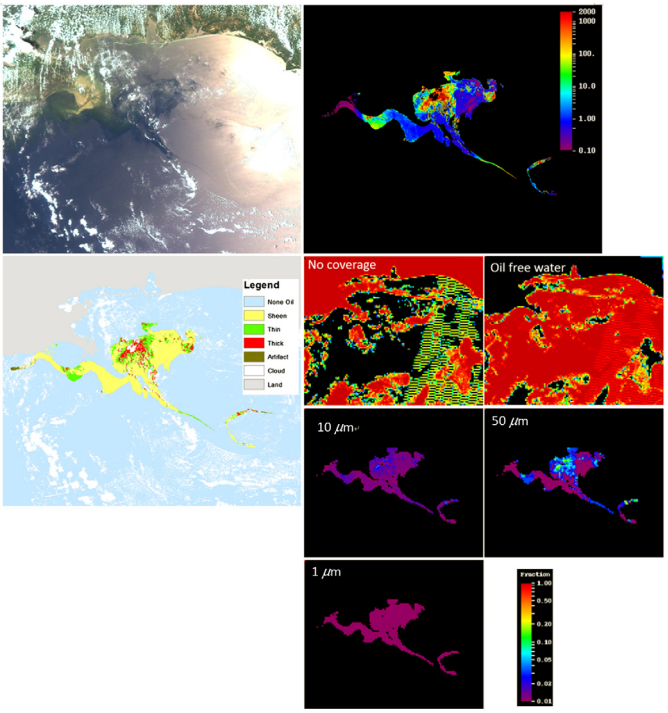


Fig. 31 May 20, 2010, 18:45 GMT. Top left: MODIS RGB image; top right: surface oil volume (liters per MODIS 250-m pixel) ("product I" in Fig. 3); bottom left: surface oil classes (sheen, thin, and thick) ("product I" in Fig. 3); bottom right: surface oil probability (e.g., 0.10 represents that 10% of the surface is covered by the corresponding class) ("product I" in Fig. 3).

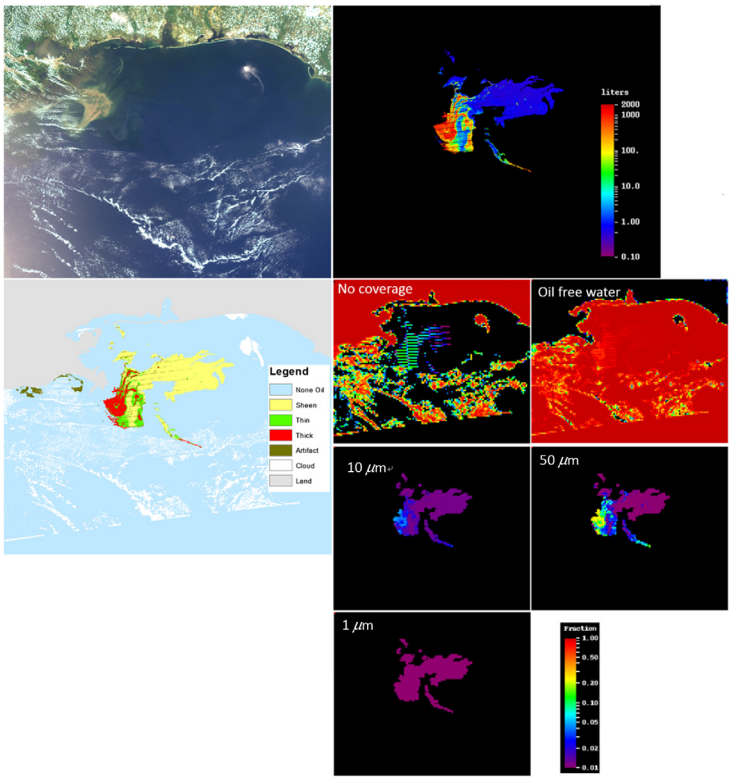


Fig. 32 May 23, 2010, 19:15 GMT. Top left: MODIS RGB image; top right: surface oil volume (liters per MODIS 250-m pixel) ("product I" in Fig. 3); bottom left: surface oil classes (sheen, thin, and thick) ("product I" in Fig. 3); bottom right: surface oil probability (e.g., 0.10 represents that 10% of the surface is covered by the corresponding class) ("product I" in Fig. 3).

Downloaded From: https://www.spiedigitallibrary.org/journals/Journal-of-Applied-Remote-Sensing on 16 Mar 2020
Terms of Use: https://www.spiedigitallibrary.org/terms-of-use

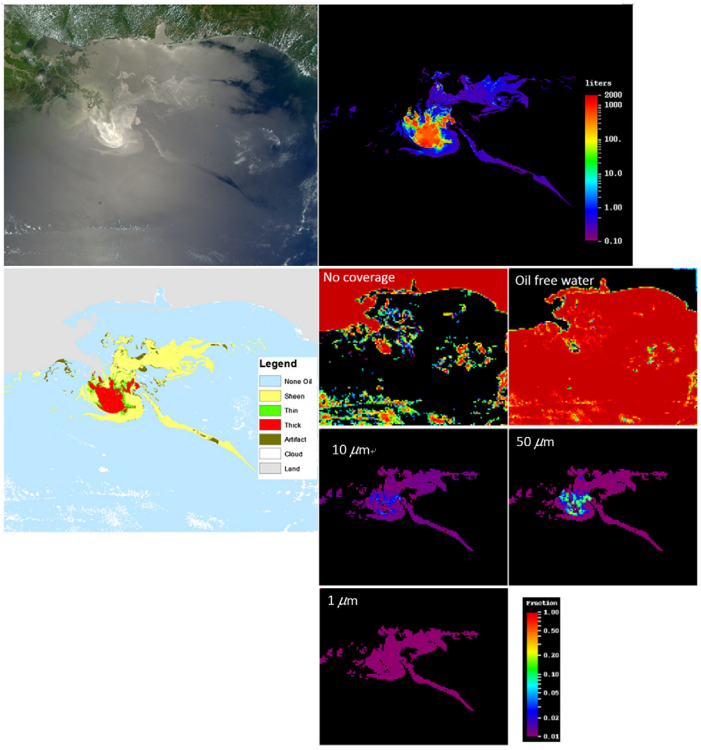


Fig. 33 May 24, 2010, 16:45 GMT. Top left: MODIS RGB image; top right: surface oil volume (liters per MODIS 250-m pixel) ("product I" in Fig. 3); bottom left: surface oil classes (sheen, thin, and thick) ("product I" in Fig. 3); bottom right: surface oil probability (e.g., 0.10 represents that 10% of the surface is covered by the corresponding class) ("product I" in Fig. 3).

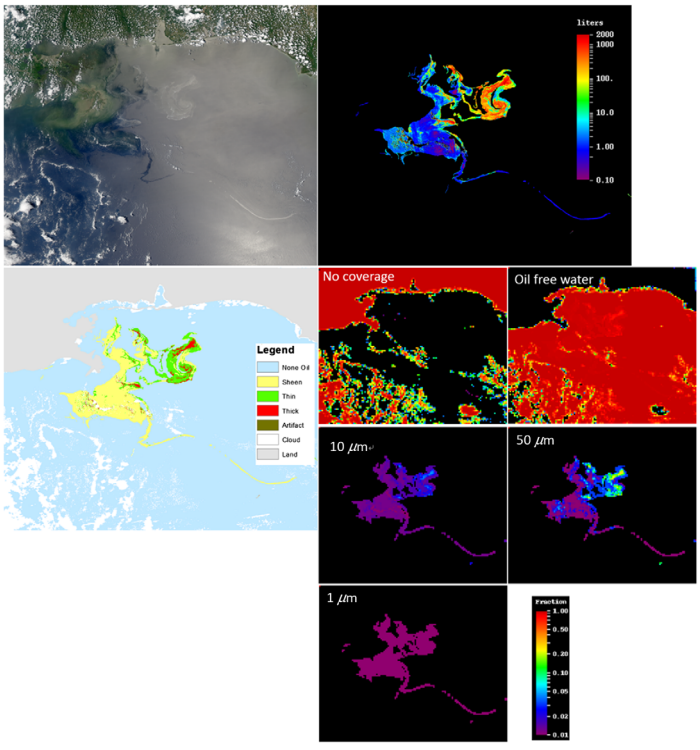


Fig. 34 April 27, 2010, 18:55 GMT. Top left: MODIS RGB image; top right: surface oil volume (liters per MODIS 250-m pixel) ("product I" in Fig. 3); bottom left: surface oil classes (sheen, thin, and thick) ("product I" in Fig. 3); bottom right: surface oil probability (e.g., 0.10 represents that 10% of the surface is covered by the corresponding class) ("product I" in Fig. 3).

Downloaded From: https://www.spiedigitallibrary.org/journals/Journal-of-Applied-Remote-Sensing on 16 Mar 2020
Terms of Use: https://www.spiedigitallibrary.org/terms-of-use

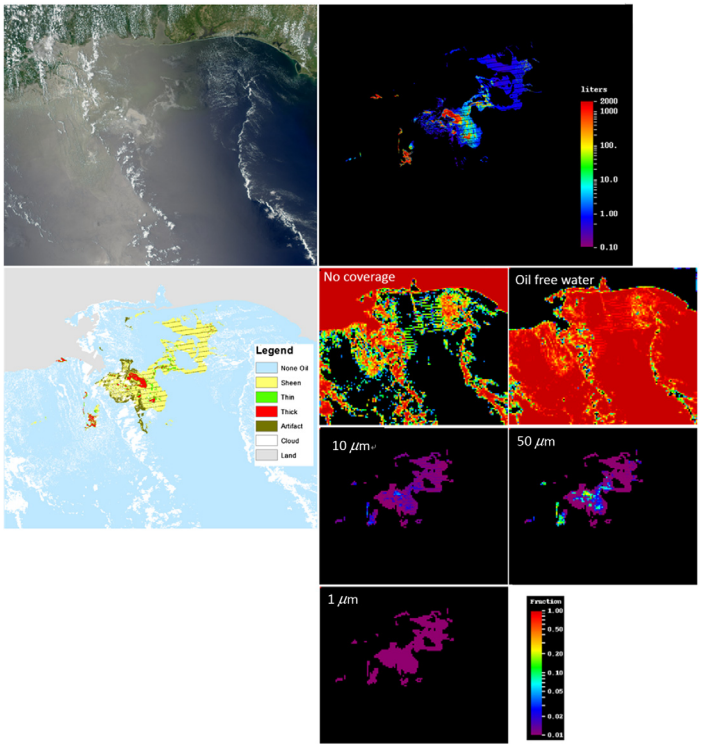


Fig. 35 June 10, 2010, 19:05 GMT. Top left: MODIS RGB image; top right: surface oil volume (liters per MODIS 250-m pixel) ("product I" in Fig. 3); bottom left: surface oil classes (sheen, thin, and thick) ("product I" in Fig. 3); bottom right: surface oil probability (e.g., 0.10 represents that 10% of the surface is covered by the corresponding class) ("product I" in Fig. 3).

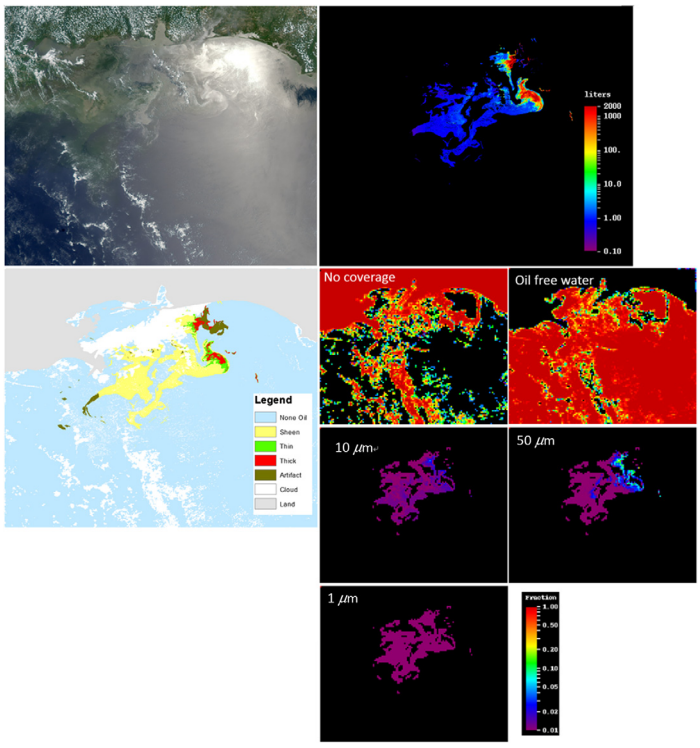


Fig. 36 June 12, 2010, 18:50 GMT. Top left: MODIS RGB image; top right: surface oil volume (liters per MODIS 250-m pixel) ("product I" in Fig. 3); bottom left: surface oil classes (sheen, thin, and thick) ("product I" in Fig. 3); bottom right: surface oil probability (e.g., 0.10 represents that 10% of the surface is covered by the corresponding class) ("product I" in Fig. 3).

Downloaded From: https://www.spiedigitallibrary.org/journals/Journal-of-Applied-Remote-Sensing on 16 Mar 2020
Terms of Use: https://www.spiedigitallibrary.org/terms-of-use

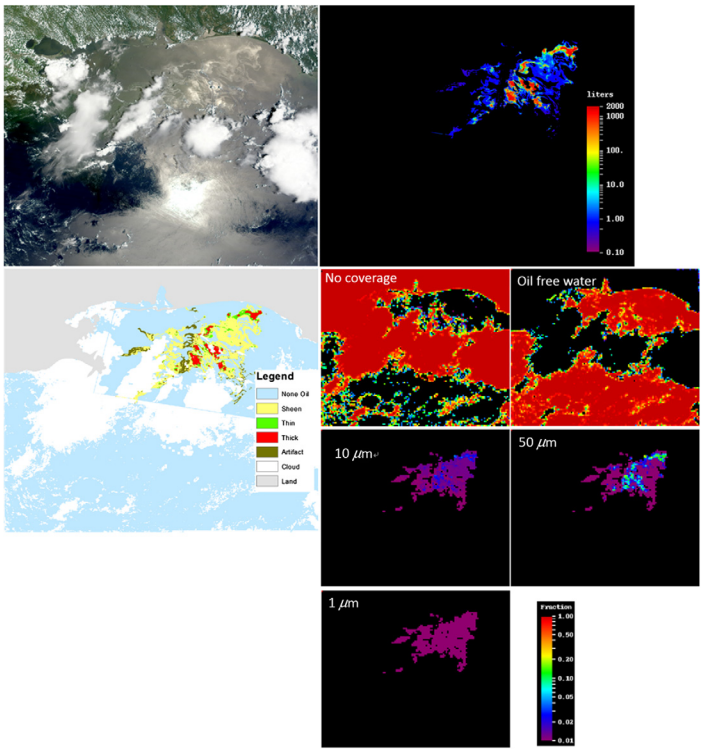


Fig. 37 June 18, 2010, 16:40 GMT. Top left: MODIS RGB image; top right: surface oil volume (liters per MODIS 250-m pixel) ("product I" in Fig. 3); bottom left: surface oil classes (sheen, thin, and thick) ("product I" in Fig. 3); bottom right: surface oil probability (e.g., 0.10 represents that 10% of the surface is covered by the corresponding class) ("product I" in Fig. 3).

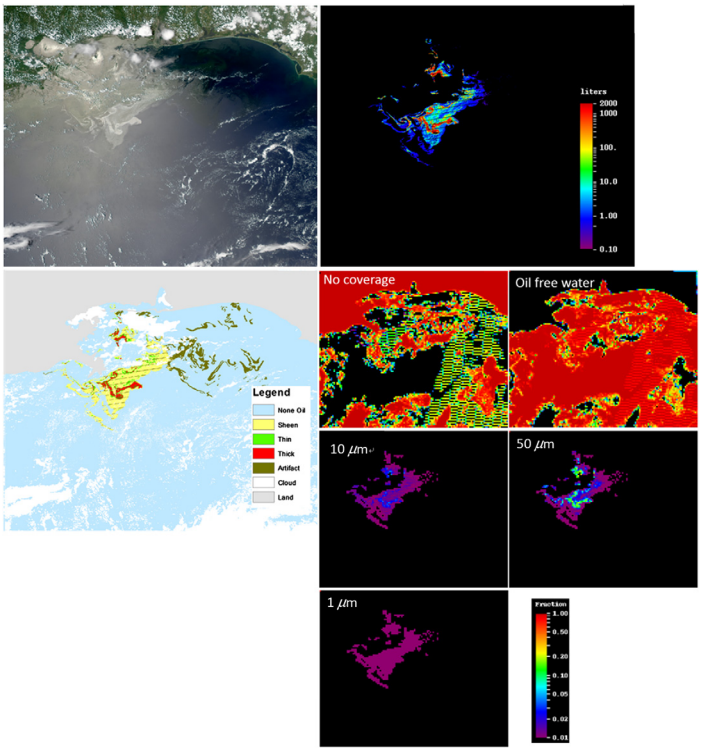


Fig. 38 June 26, 2010, 19:05 GMT. Top left: MODIS RGB image; top right: surface oil volume (liters per MODIS 250-m pixel) ("product I" in Fig. 3); bottom left: surface oil classes (sheen, thin, and thick) ("product I" in Fig. 3); bottom right: surface oil probability (e.g., 0.10 represents that 10% of the surface is covered by the corresponding class) ("product I" in Fig. 3).

Downloaded From: https://www.spiedigitallibrary.org/journals/Journal-of-Applied-Remote-Sensing on 16 Mar 2020
Terms of Use: https://www.spiedigitallibrary.org/terms-of-use

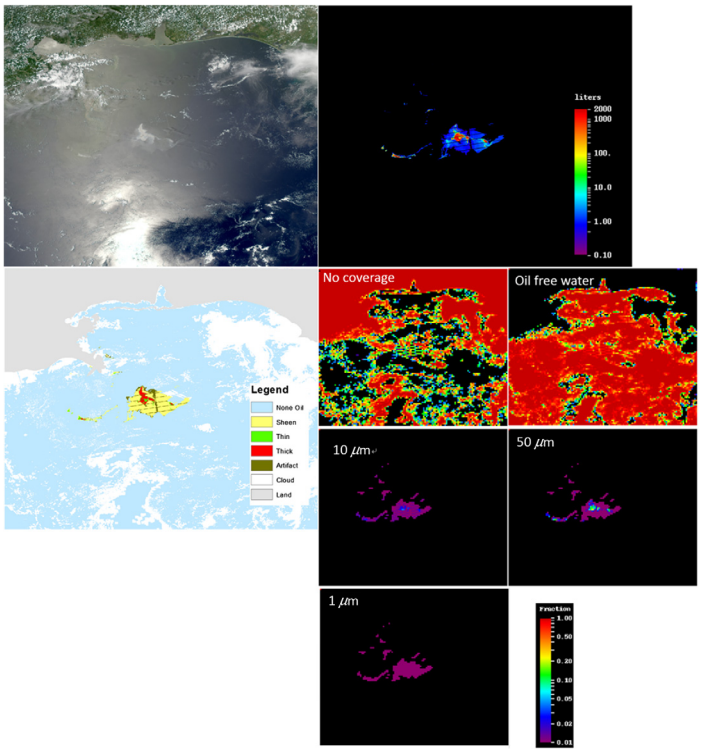


Fig. 39 July 12, 2010, 19:05 GMT. Top left: MODIS RGB image; top right: surface oil volume (liters per MODIS 250-m pixel) ("product I" in Fig. 3); bottom left: surface oil classes (sheen, thin, and thick) ("product I" in Fig. 3); bottom right: surface oil probability (e.g., 0.10 represents that 10% of the surface is covered by the corresponding class) ("product I" in Fig. 3).

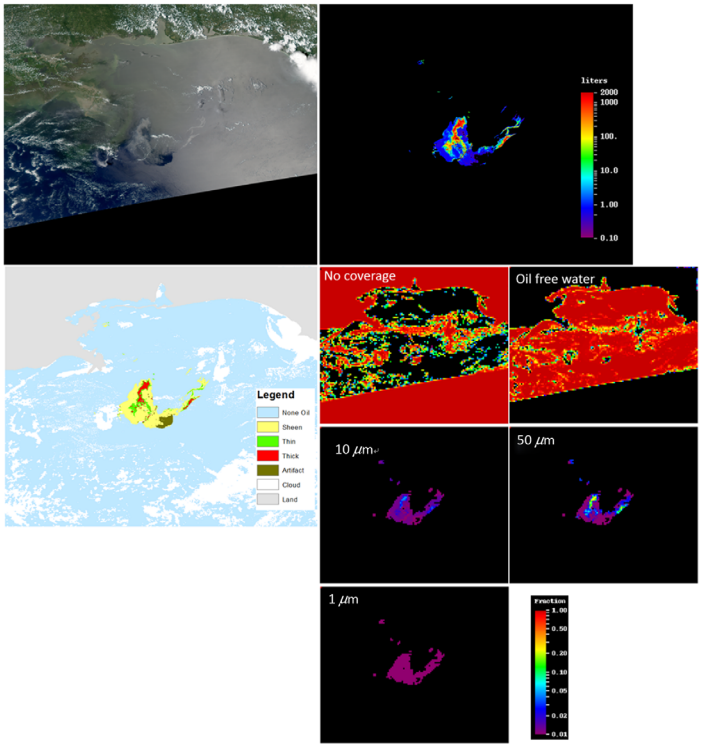


Fig. 40 July 14, 2010, 18:55 GMT. Top left: MODIS RGB image; top right: surface oil volume (liters per MODIS 250-m pixel) ("product I" in Fig. 3); bottom left: surface oil classes (sheen, thin, and thick) ("product I" in Fig. 3); bottom right: surface oil probability (e.g., 0.10 represents that 10% of the surface is covered by the corresponding class) ("product I" in Fig. 3).

Downloaded From: https://www.spiedigitallibrary.org/journals/Journal-of-Applied-Remote-Sensing on 16 Mar 2020
Terms of Use: https://www.spiedigitallibrary.org/terms-of-use

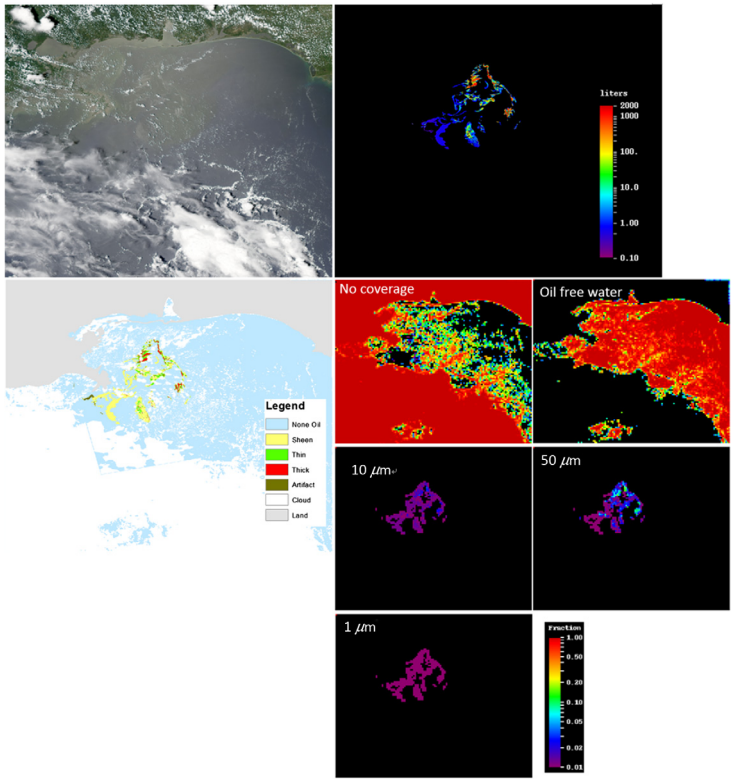


Fig. 41 July 21, 2010, 19:00 GMT. Top left: MODIS RGB image; top right: surface oil volume (liters per MODIS 250-m pixel) ("product I" in Fig. 3); bottom left: surface oil classes (sheen, thin, and thick) ("product I" in Fig. 3); bottom right: surface oil probability (e.g., 0.10 represents that 10% of the surface is covered by the corresponding class) ("product I" in Fig. 3).

Acknowledgments

This work was supported by the U.S. NASA through its Ocean Biology and Biogeochemistry program (NNX13AD08G), Biodiversity and Ecological Forecasting program (NNX14AP62A), and the U.S. Bureau of Ocean Energy Management (BOEM) Environmental Studies Program (Contract #M12PC00003). The analyses presented were also funded in part by NOAA as part of the Deepwater Horizon natural resource damage assessment and in part by the Gulf of Mexico Research Initiative through C-IMAGE. We thank the NASA GSFC, NASA JPL, and USGS, respectively, for providing MODIS and AVIRIS data. The MODIS data products, including the three types of surface oil maps, are publicly available through the Gulf of Mexico research Initiative Information & Data Cooperative (GRIIDC) at https://data.gulfresearchinitiative.org (doi: https://doi.org/10.7266/N7RJ4GGB). The remaining data images are currently not available through GRIIDC. We also thank the two reviewers for providing extensive comments and suggestions to help improve the presentation of this paper. Any use of trade, firm, or product names is for descriptive purposes only and does not imply endorsement by the U.S. Government.

References

1. U. C. Guard, "On scene coordinator report on Deepwater Horizon oil spill," Vol. 10, http://www.uscg.mil/foia/docs/dwh/fosc_dwh_report.pdf (October 2011).
2. United States of America v. BP Exploration and Production, Inc., "Findings of fact and conclusions of law: phase two trial. In re: oil spill by the oil rig 'Deepwater Horizon' in the Gulf of Mexico, on April 20, 2010, No. MDL 2179, 2015 WL 225421 (LA. E.D. Jan. 15, 2015). (Doc. 14021)," U.S. District Court for the Eastern District of Louisiana, 2015, http://www.laed.uscourts.gov/OilSpill/Orders/1152015FindingsPhaseTwo.pdf (January 2015).

Downloaded From: https://www.spiedigitallibrary.org/journals/Journal-of-Applied-Remote-Sensing on 16 Mar 2020
Terms of Use: https://www.spiedigitallibrary.org/terms-of-use

3. M. K. McNutt et al., "Review of flow rate estimates of the Deepwater Horizon oil spill," *Proc. Natl. Acad. Sci. U. S. A.* **109**(50), 20260–20267 (2012).
4. I. Leifer et al., "State of the art satellite and airborne marine oil spill remote sensing: application to the BP Deepwater Horizon oil spill," *Remote Sens. Environ.* **124**, 185–209 (2012).
5. O. Garcia-Pineda et al., "Detection of floating oil anomalies from the Deepwater Horizon oil spill with synthetic aperture radar," *Oceanography* **26**(2), 124–137 (2013).
6. O. Garcia-Pineda et al., "Oil spill mapping and measurement in the Gulf of Mexico with textural classifier neural network algorithm (TCNNA)," *IEEE J. Sel. Top. Appl. Earth Obs. Remote Sens.* **6**(6), 2517–2525 (2013).
7. I. R. MacDonald et al., "Natural and unnatural oil slicks in the Gulf of Mexico," *J. Geophys. Res.: Oceans* **120**(12), 8364–8380 (2015).
8. C. Hu, "An empirical approach to derive MODIS ocean color patterns under severe sun glint," *Geophys. Res. Lett.* **38**, 1603 (2011).
9. Y. Liu et al., "Tracking the Deepwater Horizon oil spill: a modeling perspective," *Eos Trans. AGU* **92**(6), 45–52 (2011).
10. Y. Liu et al., "Trajectory forecast as a rapid response to the Deepwater Horizon oil spill, in monitoring and modeling the Deepwater Horizon oil spill: a record-breaking enterprise," *Geophys. Monogr. Ser.* **195**, 153–165 (2011).
11. S. Sun et al., "Oil slick morphology derived from AVIRIS measurements of the Deepwater Horizon oil spill: implications for spatial resolution requirements of remote sensors," *Mar. Pollut. Bull.* **103**(1–2), 276–285 (2016).
12. R. N. Clark et al., "A method for quantitative mapping of thick oil spills using imaging spectroscopy," U.S. Geological Survey Open-File Report 2010–1167, pp. 1–51, U.S. Geological Survey (2010).
13. R. S. Rand, R. N. Clark, and K. E. Livo, "Feature-based and statistical methods for analyzing the Deepwater Horizon oil spill with AVIRIS imagery," *Proc. SPIE* **8158**, 81580N (2011).
14. T. Lammoglia and C. R. de Souza Filho, "Spectroscopic characterization of oils yielded from Brazilian offshore basins: potential applications of remote sensing," *Remote Sens. Environ.* **115**(10), 2525–2535 (2011).
15. T. Lammoglia and C. R. de Souza Filho, "Mapping and characterization of the API gravity of offshore hydrocarbon seepages using multispectral ASTER data," *Remote Sens. Environ.* **123**, 381–389 (2012).
16. T. Lammoglia and C. R. de Souza Filho, "Chronology and backtracking of oil slick trajectory to source in offshore environments using ultraspectral to multispectral remotely sensed data," *Int. J. Appl. Earth Obs. Geoinf.* **39**, 113–119 (2015).
17. J. Svejkovsky and J. Muskat, "Real-time detection of oil slick thickness patterns with a portable multispectral sensor," Final Report submitted to the U.S. Department of the Interior, p. 77, Mineral Management Service, Herndon, Virginia (2006).
18. M. Fingas, "How to measure slick thickness (or not)," in *Proc. of the 35th Arctic and Marine Oil spill Program Technical Seminar* (2012).
19. M. Fingas and C. Brown, "Response to Svejkovsky et al.," *Mar. Pollut. Bull.* **93**(1–2), 298–300 (2015).
20. J. Svejkovsky et al., "Rebuttal to published article 'review of oil spill remote sensing' by M. Fingas and C. Brown," *Mar. Pollut. Bull.* **93**(1–2), 294–297 (2015).
21. C. Brekke and A. H. Solberg, "Oil spill detection by satellite remote sensing," *Remote Sens. Environ.* **95**(1), 1–13 (2005).
22. M. N. Jha, J. Levy, and Y. Gao, "Advances in remote sensing for oil spill disaster management: state-of-the-art sensors technology for oil spill surveillance," *Sensors* **8**(1), 236–255 (2008).
23. M. Jacobi et al., "Environmental response management application," in *Int. Oil Spill Conf.*, American Petroleum Institute (2008).
24. O. Garcia-Pineda et al., "Using SAR images to delineate ocean oil slicks with a texture-classifying neural network algorithm (TCNNA)," *Can. J. Remote Sens.* **35**(5), 411–421 (2009).
25. M. Adamo et al., "Detection and tracking of oil slicks on sun-glittered visible and near infrared satellite imagery," *Int. J. Remote Sens.* **30**(24), 6403–6427 (2009).

Downloaded From: https://www.spiedigitallibrary.org/journals/Journal-of-Applied-Remote-Sensing on 16 Mar 2020
Terms of Use: https://www.spiedigitallibrary.org/terms-of-use

26. C. Hu et al., "Detection of natural oil slicks in the NW Gulf of Mexico using MODIS imagery," *Geophys. Res. Lett.* **36**, L01604 (2009).
27. C. Hu, X. Li, and W. G. Pichel, "Detection of oil slicks using MODIS and SAR imagery," in *Handbook of Satellite Remote Sensing Image Interpretation: Applications for Marine Living Resources Conservation and Management*, J. Morales et al., Eds., pp. 21–34, EU PRESPO and IOCCG, Dartmouth, Canada (2011).
28. C. Hu et al., "MODIS detects oil spills in Lake Maracaibo, Venezuela," *Eos Trans. AGU* **84**(33), 313–319 (2003).
29. C. Hu et al., "Did the northeastern Gulf of Mexico become greener after the Deepwater Horizon oil spill?" *Geophys. Res. Lett.* **38**, 9601 (2011).
30. I. MacDonald et al., "Natural oil slicks in the Gulf of Mexico visible from space," *J. Geophys. Res.* **98**(C9), 16351–16364 (1993).
31. J. Zhao et al., "Exploring the potential of optical remote sensing for oil spill detection in shallow coastal waters-a case study in the Arabian Gulf," *Opt. Express* **22**(11), 13755–13772 (2014).
32. I. R. MacDonald et al., "Remote sensing inventory of active oil seeps and chemosynthetic communities in the northern Gulf of Mexico," in *Hydrocarbon Migration and its Near-Surface Expression*, D. Schumacher and M. A. Abrams, Eds., American Association of Petroleum Geologists Memoir, Vol. **66**, pp. 27–37, American Association of Petroleum Geologists, Tulsa, Oklahoma (1996).
33. G. Chust and Y. Sagarminaga, "The multi-angle view of MISR detects oil slicks under sun glitter conditions," *Remote Sens. Environ.* **107**(1), 232–239 (2007).
34. J. Svejkovsky et al., "Characterization of surface oil thickness distribution patterns observed during the Deepwater Horizon (MC-252) oil spill with aerial and satellite remote sensing," *Mar. Pollut. Bull.* **110**(1), 162–176 (2016).
35. Y. Lu et al., "Determining oil slick thickness using hyperspectral remote sensing in the Bohai Sea of China," *Int. J. Digital Earth* **6**(1), 76–93 (2013).
36. J. Svejkovsky et al., "Operational utilization of aerial multispectral remote sensing during oil spill response," *Photogramm. Eng. Remote Sens.* **78**(10), 1089–1102 (2012).
37. J. Svejkovsky and J. Muskat, "Development of a portable multispectral aerial sensor for real-time oil spill thickness mapping in coastal and offshore waters," Final Report for US Minerals Management Service Contract M07PC13205, p. 33, U.S. Department of the Interior, Herndon, Virginia (2009).
38. M. Wettle et al., "Assessing the effect of hydrocarbon oil type and thickness on a remote sensing signal: a sensitivity study based on the optical properties of two different oil types and the HYMAP and Quickbird sensors," *Remote Sens. Environ.* **113**(9), 2000–2010 (2009).
39. S. Angelliaume et al., "Hyperspectral and radar airborne imagery over controlled release of oil at sea," *Sensors* **17**(8), 1772 (2017).
40. Z. Otremba, "Oil-in-water emulsion as a modifier of water reflectance," *Opt. Appl.* **39**, 123–128 (2009).
41. Z. Otremba and J. Piskozub, "Modelling of the optical contrast of an oil film on a sea surface," *Opt. Express* **9**(8), 411–416 (2001).
42. Z. Otremba and J. Piskozub, "Modeling the remotely sensed optical contrast caused by oil suspended in the sea water column," *Opt. Express* **11**(1), 2–6 (2003).
43. Z. Otremba, O. Zielinski, and C. Hu, "Optical contrast of oil dispersed in seawater under windy conditions," *J. Eur. Opt. Soc.–Rapid Publ.* **8**, 13051 (2013).
44. T. Król, A. Stelmaszewski, and W. Freda, "Variability in the optical properties of a crude oil-seawater emulsion," *Oceanologia* **48**(S), 203–211 (2006).
45. G. De Carolis, M. Adamo, and G. Pasquariello, "On the estimation of thickness of marine oil slicks from sun-glittered, near-infrared MERIS and MODIS imagery: the Lebanon oil spill case study," *IEEE Trans. Geosci. Remote Sens.* **52**(1), 559–573 (2014).
46. D. Dubucq et al., "Detection and discrimination of the thick oil patches on the sea surface," in *ISPRS-Int. Archives of the Photogrammetry, Remote Sensing and Spatial Information Sciences*, pp. 417–421 (2016).
47. https://aviris.jpl.nasa.gov/alt_locator/ (July 2012).

Downloaded From: https://www.spiedigitallibrary.org/journals/Journal-of-Applied-Remote-Sensing on 16 Mar 2020
Terms of Use: https://www.spiedigitallibrary.org/terms-of-use

48. R. N. Clark et al., "Imaging spectroscopy: earth and planetary remote sensing with the USGS Tetracorder and expert systems," *J. Geophys. Res. (Planets)* **108**, 5131 (2003).
49. C. Hu et al., "Dynamic range and sensitivity requirements of satellite ocean color sensors: learning from the past," *Appl. Opt.* **51**(25), 6045–6062 (2012).
50. C. Pohl and J. L. Van Genderen, "Review article: multisensor image fusion in remote sensing: concepts, methods and applications," *Int. J. Remote Sens.* **19**(5), 823–854 (1998).
51. M. Wang and C. Hu, "Extracting oil slick features from VIIRS nighttime imagery using a Gaussian filter and morphological constraints," *IEEE Geosci. Remote Sens. Lett.* **12**(10), 2051–2055 (2015).
52. S. Ackerman et al., *Discriminating Clear-Sky from Cloud with MODIS Algorithm Theoretical Basis Document (MOD35)*, MODIS Cloud Mask Team, Cooperative Institute for Meteorological Satellite Studies, University of Wisconsin, Madison, Wisconsin (2010).
53. C. Hu, K. L. Carder, and F. E. Muller-Karger, "Atmospheric correction of SeaWiFS imagery over turbid coastal waters: a practical method," *Remote Sens. Environ.* **74**(2), 195–206 (2000).
54. C. Hu and L. Feng, "GOES imager shows diurnal changes of a trichodesmium erythraeum bloom on the West Florida shelf," *IEEE Geosci. Remote Sens. Lett.* **11**(8), 1428–1432 (2014).
55. Bonn Agreement, "Bonn agreement aerial operations handbook," 2009, www.bonnagreement.org (1 June 2012).
56. J. Hollinger and R. Mennella, "Oil spills: measurements of their distributions and volumes by multifrequency microwave radiometry," *Science* **181**(4094), 54–56 (1973).
57. R. G. Congalton and K. Green, *Assessing the Accuracy of Remotely Sensed Data: Principles and Practices*, CRC Press, New York, New York (2008).
58. R. G. Congalton, "A review of assessing the accuracy of classifications of remotely sensed data," *Remote Sens. Environ.* **37**(1), 35–46 (1991).
59. M. Story and R. G. Congalton, "Accuracy assessment-a user's perspective," *Photogramm. Eng. Remote Sens.* **52**(3), 397–399 (1986).
60. V. F. Labson et al., "Estimated minimum discharge rates of the deepwater horizon spill—interim report to the flow rate technical group from the mass balance team," U.S. Geological Survey Open-File Report 2010-1132, pp. 1–8, U.S. Geological Survey http://pubs.usgs.gov/of/2010/1132/pdf/OF10-1132.pdf (2010).
61. S. Cheemalapati et al., "Measurement of thickness of highly inhomogeneous crude oil slicks," *Appl. Opt.* **56**(11), E72–E76 (2017).
62. S. Sun and C. Hu, "On the challenge of remote estimation of surface oil volume in the ocean: examples from satellite and airborne measurements," in *GoMRI Oil Spill & Ecosystem Science Conf.*, Houston, Texas (2015).

Chuanmin Hu received his BS degree in physics from the University of Science and Technology of China, Hefei, China, 1989, and received his PhD in physics (ocean optics) from the University of Miami, Coral Gables, Florida, USA, 1997. Currently, he is a professor at the College of Marine Science, University of South Florida, St. Petersburg, Florida, USA, where he is also the Director of the Optical Oceanography Laboratory (http://optics.marine.usf.edu).

Lian Feng received his PhD in cartography and geography information system from Wuhan University, Wuhan, China, 2013. He was a postdoctoral associate with the Optical Oceanography Laboratory, College of Marine Science, University of South Florida, USA, between 2015 and 2017. Currently, he is an assistant professor with the School of Environmental Science and Engineering, Southern University of Science and Technology, China.

Jamie Holmes is a principal scientist/vice president at Abt Associates in Boulder, Colorado, where he leads a natural resource damage assessment practice. He co-led the group of remote sensing experts who evaluated the extent of the Deepwater Horizon oil spill. His team has been developing new methods of quantifying oil slicks in open water. He received his MS degree in earth sciences from Dartmouth College and his BA in environmental biology from Middlebury College.

Downloaded From: https://www.spiedigitallibrary.org/journals/Journal-of-Applied-Remote-Sensing on 16 Mar 2020
Terms of Use: https://www.spiedigitallibrary.org/terms-of-use

Gregg A Swayze received his PhD in geology from the University of Colorado at Boulder in 1997. He has worked as a research geophysicist for the U.S. Geological Survey since 1985, specializing in imaging spectroscopy of mine waste, naturally occurring asbestos, Mars surface mineralogy, hydrothermal alteration, rare earth minerals, and disaster sites. He is a scientific collaborator with the NASA Mars Reconnaissance Orbiter CRISM team and a member of the NASA EMIT imaging spectrometer team.

Ira Leifer received a BS degree in astronomy and physics from SUNY Stony Brook, and a PhD from Georgia Institute of Technology in Earth and Atmospheric Sciences. He was a research associate at the University of California, Santa Barbara for 15 years. Currently, he is CEO of Bubbleology Research International, a small environmental consulting technology development company. He is the academic representative of FOSTERRS, a NASA led interagency working group on oil spill remote sensing.

Christopher Melton received a BS in physics with a specialization in earth sciences from the University of California, San Diego, 2005 and a MS degree in physical oceanography from the University of California, Santa Barbara, 2008. He worked at UCSB's Earth Research Institute until 2010 and is currently working as a data analyst at Bubbleology Research International.

Oscar Garcia received a BS in electrical engineering from the Instituto Tecnologico de Ciudad Madero, Mexico; he also received a MS degree in Geoscience from Instituto de Estudios Superiores de Tamaulipas, and then a PhD in coastal and marine sciences from Texas A&M University, Corpus Christi. He is the director of Water Mapping, LLC, a consultant company dedicated to provide aerial and satellite mapping services.

Ian MacDonald is a professor of oceanography at Florida State University. He earned his PhD from Texas A&M University and has published discovery papers on remote sensing of natural oil slicks, deep-sea brine pools, gas hydrates, mud volcanoes, and asphalt ecosystems. At the onset of the BP oil spill, he correctly estimated that the rate of discharge exceeded 27,500 barrels per day.

Mark Hess received a BS degree in aquatic biology from the University of California at Santa Barbara and a master in business administration from Colorado State University. He is the director of operations for Ocean Imaging, Inc. a small environmental research and consulting company specializing in coastal and oceanic remote sensing science. He has worked at Ocean Imaging for over 29 years.

Frank Muller-Karger has a BS degree from the Florida Institute of Technology in 1979, a MS degree in oceanography from the University of Alaska Fairbanks in 1984, a PhD in marine and estuarine sciences from the University of Maryland in 1988, and a MS in management from the University of South Florida in 2001. He is the director of the Institute for Marine Remote Sensing at the College of Marine Science, University of South Florida (http://imars.usf.edu).

George Graettinger received his BA degree in geology from Knox College, Galesburg, Illinois in 1984. He is an environmental scientist for NOAA Office of Response and Restoration (OR&R) in Seattle, Washington. He is a senior GIS project manager for OR&R with experience in remediation, natural resource damage assessment, data analysis, remote sensing, and the development of GIS-based decision support systems. He is the Gulf of Mexico Regional lead for the environmental response management application (ERMA).

Rebecca Green received her BS degree in 1994 from the California Institute of Technology (Caltech) and her PhD in biological oceanography in 2002 from the M.I.T./Woods Hole Oceanographic Institution (WHOI) Joint Program, specializing in ocean optics. She is currently a senior oceanographer with the U.S. Department of Interior's Bureau of Ocean Energy Management (BOEM) in the Gulf of Mexico Regional Office in New Orleans, where she has worked since 2010.

Downloaded From: https://www.spiedigitallibrary.org/journals/Journal-of-Applied-Remote-Sensing on 16 Mar 2020
Terms of Use: https://www.spiedigitallibrary.org/terms-of-use